POSE ESTIMATION AND MATERIAL REMOVAL STUDY OF A NON-RIGID ENDOSCOPIC MACHINING TOOL

A THESIS SUBMITTED TO THE GRADUATE DIVISION OF THE UNIVERSITY OF HAWAI‘I AT MĀNOA IN PARTIAL FULFILLMENT OF THE REQUIREMENTS FOR THE DEGREE OF

MASTER OF SCIENCE

IN

MECHANICAL ENGINEERING

AUGUST 2011

By
Yang Lei

Thesis Committee:

Scott Miller, Chairperson
Brian Bingham
Peter Berkelman

We certify that we have read this thesis and that, in our opinion, it is satisfactory in scope and quality as a thesis for the degree of Master of Science in Mechanical Engineering.

THESIS COMMITTEE

_____

Chairperson

_____

_____

Table of Contents

List of Tables

List of Figures

Abstract

There is currently no efficient way to quantitatively (precisely) remove material from work pieces in hard-to-reach cavities, such as turbine blades in a jet engine. There is a need to be able to smooth the cracks from the turbine blades with a controlled amount of material removal. Endoscopy is useful for navigating and inspecting features in internal cavities with a flexible body and a semi-rigid bending section. By turning control knobs on the endoscope, the bending section can access a workpiece on its lateral direction. In this research, it is hypothesized that an endoscope can be used to remotely grind a predetermined amount of material and smooth the cracks on a work piece. The research objectives are to set up a precise flexible machining operation and to measure the accuracy of the estimated amount of material that can be removed. Experiment results shows that a reasonable accuracy was achieved using a modified flexible medical endoscope.

In this study, two models were built to estimate the pose (position and orientation) and force on a modified PENTAX ES-3801 endoscope. The pose model was based on geometric analysis of the endoscope bending section. When the internal force was compensated in calculation, the average pose estimation error was less than 4 mm of distance and 5 degrees of bending angle. The force model was based on equilibrium analysis of the bending section and the average force prediction error was 0.5 N in the range of 1 to 8 N. The experimental and estimated results prove that the pose and force of the flexible bending section can be predicted and monitored when subjected to varying loads from work piece.

In grinding processes, self-excited vibration (chatter) will seriously degrade the geometric accuracy and surface finish of the workpiece. The proposed endoscopic machining tool is naturally vulnerable to chatter due to its high degrees of freedom and low structural rigidity. A dynamic model was built to study the self-excited vibration characteristics of the endoscopic machining tool. By analyzing the stability lobe diagram (SLD), optimized machining parameters were found to reduce the chatter. An on-line chatter detecting method is proposed to identify self-excited vibration in its early stage.

Finally, a material removal rate (MRR) model was formulated to predict the amount of material removal in this endoscopic grinding process. By calculating the energy wasted by chatter and the effective energy spent on grinding, the MRR was predicted. Several machining experiments were conducted to validate the repeatability of the model and evaluate its accuracy. The average MRR prediction error is 22% related to the measured MRR.

Experiment results reveals that the current MRR prediction accuracy (in the scale of 0.5 mg) is not high enough to meet industry requirement, which is believed to be 0.004 mg for sub-millimeter size cracks. Recommendations of improving pose estimation and MRR prediction accuracies such as designing a more predictable endoscopic tool structure, using a sphere grinding tool head and adopting a pneumatic driving mechanism or tip mounted motor are proposed.

Chapter 1

Introduction

1.1 Research Motivation

There is currently no effective way to quantitatively remove material from internal components of engineered cavities. Current machine tools have a relatively massive base and are considered to be a sufficiently rigid system, i.e., the deflection of the machining base and tool are negligible and the MRR can be easily quantified from the tool movement. However, they are too big to conduct machining tasks in engineered cavities. Endoscopic tools have been patented for blending or smoothing defects on a turbine blade [1][2][3], however these instruments do not allow precise guidance during working operation [2]. These tools are not built for quantitative material removing and the machining process can only be monitored by visual means, which is imprecise and inadequate. A major need is to be able to inspect and remove a known amount of material with application specified precision (say 0.004 mg for smoothing sub-millimeter cracks) from the blade of a turbine engine, such as those used in aircraft or power plants, during a maintenance operation without having to undertake time consuming and therefore expensive dismantling and reassembly [2]. To repair damaged blades, the engine has to be removed, requiring up to 850 hours of labor and costing as much as $500,000 adding up to more than $10 million in maintenance costs per year [4].

The cracks can be caused by foreign objects, such as sand particles or stones in the shape of V-shaped nicks or chips on impact along the leading edge, as shown in Fig.1.1(b). Their size is limited to a few tenths of a millimeter [3]. According to Seng [5], an initial 0.2 inch (radius) crack on the TF41-A-1B fan disk can grow up to 0.58 inch (radius) after 4474 engine power cycles without catastrophic failure in a seeded fault test. During a maintenance operation, in order to prevent such notches or nicks from becoming more pronounced and potentially cracking the turbine blade, it is desirable to detect them early and, if possible, repair or blend the defects [1]. The current methods

of polishing or grinding these cracks are cumbersome and impractical, and there are no adequate tools for these operations.

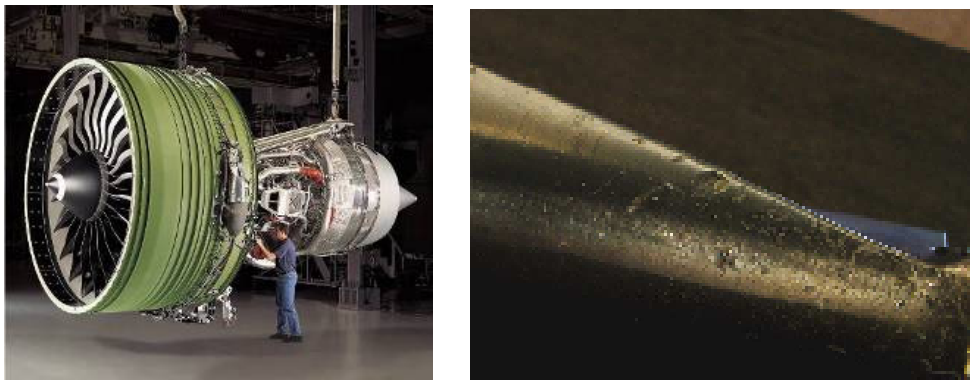

(a) GE90 aircraft engine (Defense 2009) (b) Cracked turbine blade (Carter 2005)

Figure 1.1. Target application for endoscopic machining

It would be advantageous if an endoscope could be used to detect interior flaws of a complex structure and perform a machining operation (grinding, polishing, deburring, etc.) to repair them in a single step. Figure 1.2 shows the concept and setup of endoscope machining. The balloon supports the base of endoscope bending section against the cavity. A small grinding tool is connected to an external motor through a flexible steel cable. An aluminum workpiece is fixed on a dynamometer that measures machining forces.

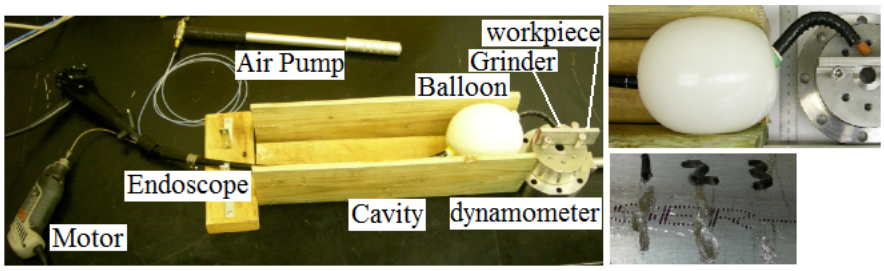

Figure 1.2. Endoscopic machining experiment and grinding marks on aluminum workpiece

In the application scenarios regarding jet engine turbine blade cracks smoothing, a good accuracy of material removal is believed to be a fraction of 0.001 mm^3 to 1.0 mm^3 in volume [3][5] or 0.004 mg to 4.0 mg in mass (densities of Nickel, Titanium, and Aluminum are 8.91, 4.56 and 2.70 g/cm^3 respectively), which sets the target of accuracy of non-rigid endoscopic machining.

The major issue of this research is quantifying the material removal from a non-rigid machining system. The accuracy of a flexible machining system is unknown when the tool deflection is significant in the machining operation. Before endoscopic tools can carry out force critical machining tasks such as grinding, several fundamental studies have to be done to determine their capabilities.

1.2 Background

1.2.1 Endoscopy

Endoscopy as a technique of examining internal cavities of the human body were born in 19th century [6]. The term "endoscope" was first used by a French surgeon, Antonin Jean Desormeaus (1844-1894) in 1853, but the ancestor of the modern endoscope, the "Lichtleiter" was designed by Philip Bozzini(1773-1809) in Vienna in 1796.

In contemporary medical practice, endoscope and endoscopy were developed into several subtypes bearing different designs, structures and specialties. Thus, terminology was derived, such as gastroscopy, colonoscopy, cystoscopy, laparoscopy, proctoscopy, rhinoscopy, thoracoscopy etc.

Structurally, a flexible endoscope comprises three parts – a handler with two independent lockable control knobs bearing sprocket-chain or wheel-cable driving mechanism, a long flexible hollow shaft having driving chains (cables) and same other internal channels running through it and to the tip of a bending section. By turning two control knobs, the operator could bend the bending section to any angle within its workspace. The endoscope used in this study is shown in figure 1.3 (Model PENTAX ES-3801), which has a diameter of 11.3 mm with a 3.5 mm channel biopsy port, 120^o angle of view, 70 cm working length, and angulation of $\pm 180^o$ up/down and $\pm 160^o$ right/left. It contains channels for light, viewing, air/water, and an operating channel. The operating channel (usually 2-4 mm in diameter) allows the passage of fine flexible accessories (grinding tool in our experiments) from a port on the endoscope control head through the shaft and into the field of view.

1.2.2 Industrial application

As mentioned above, there is a lens port on the tip of the endoscope bending section, which provides a wide angle of view. Therefore, besides medical practice, endoscopes are widely applied in many other fields. For example, in the chemical and petrochemical industry, endoscopes are used to inspect pipelines, pressure vessels and heat exchangers. In aircraft and space industry,

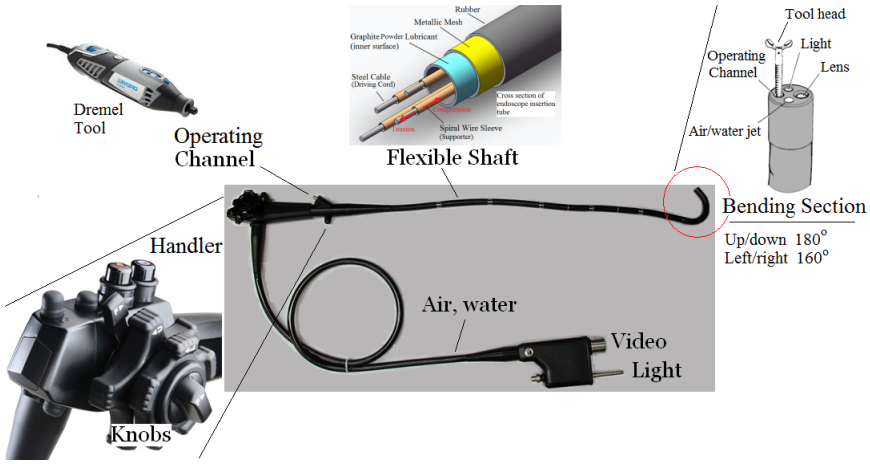

Figure 1.3. PENTAX ES-3801 endoscope

they are used to inspect turbine and compressor blades, air-gas channels, casings, sprayers and combustor burners. In shipyards, endoscopes are used for the inspection of diesel and electric engines, generators and power transmission mechanisms [7]. Some other applicable areas include, rail and transport, automobile industry, architecture and building, and energetics. However, most tasks are not force-critical. Therefore the deflection and deformation of the endoscope is not a liability.

1.2.3 State-of-the-art in machining and machine tools

Currently, the conventional rigid machine tools have the highest rigidity and highest repeatability and accuracy. For example, the Hass TL-4 computer numerical control (CNC) machine center, has a repeatable accuracy of ± 0.005 mm. Semi-rigid tools sacrifice some rigidity to achieve higher flexibility. For example, the Yaskawa Motorman EH80 robot has the theoretical repeatable accuracy of ± 0.07 mm. In contrast, the non-rigid machining tools, such as a Dremel tool held by a human being, is likely to have a repeatable accuracy of ± 1.0 mm.

1.3 Literature Review

1.3.1 Endoscopic Machining Techniques

As mentioned above, patents have been issued for smoothing cracks, nicks, and defects. In Moeller et al.'s design [1], the grinding head was fixed by articulating an outer portion (64b)

of the support tube, as shown in figure 1.4(a). Desgranges et al. [3] patented a tool supported by exterior means, as shown in figure 1.4(b). Both of the patented instruments seem to have been designed for specific applications and have shortcomings. Firstly, the operation is imprecise, i.e., the amount of material removal and positioning are not known. Secondly, the material removal can only be estimated qualitatively by visual means. The fixturing methods are limited to either external or application specific. Thirdly, the depth of penetration into the cavity seems to be limited to less than 1 m in most cases.

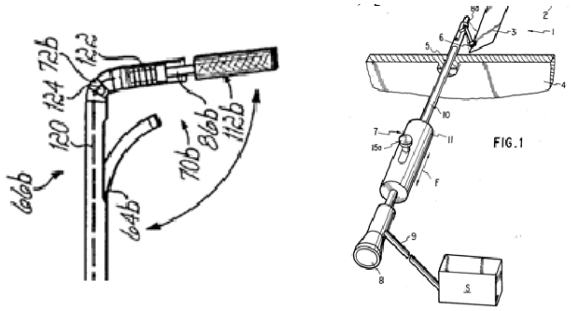

(a) Moeller et al., 2005 (b) Desgranges et al., 1992

Figure 1.4. Patented endoscopic grinding tools

Arai et al. [8] presented a concept of an endoscope that had two air suction grippers to latch onto skin, and an electrical scalpel, both actuated by shape memory alloy. However, the concept was not developed and this study was limited to experiments on shape memory actuation of a microarm.

For the fixturing of the bending section inside a cavity, the balloon fixture method has been proposed. Hussein [9] patented an endoscopic device with an inflatable balloon near the tip of the endoscope. The purpose of the balloon was to provide an unobstructed view within the body space of a patient by clearing opaque fluid and debris from the lens of the viewing system. It was acknowledged that the balloon could provide structural support and proper spacing between the terminal end of the viewing system and the lumen site being inspected for proper focus. In future research, a similar idea should be pursued for a means to fix the tip of the endoscope in place at the base of the bending section.

Fujinon [10] and Olympus [11] have developed a double and single ballooning system, respectively. These fixtures operate with the use of an external splinting tube, which slides over the endoscope and is inflated and controlled by a pump. Used to explore, diagnose, and treat the gastrointestinal tract, it fixes itself by expanding and pushing outward on the gastrointestinal wall.

Once in the small intestines, it is pulled back outward to compress the intestines, deflated, and then advanced again, allowing for greater insertion depths. These ballooning systems are only utilized for navigating the gastrointestinal track. The concept of an extendable, flexible fixture is new and unexplored, but this is not the major focus of this research.

1.3.2 Machining from Flexible Robotic Arms

The flexibility of long arms has been studied in robotic machining and control of manipulators. Raibert and Craig [12] described a hybrid technique where force and torque information were combined with positional data for control of robotic manipulators. Akbari and Higuchi [13] use external cutting force data to adjust the tool to the workpiece surface in a grinding operation by a six axis articulated robot. Matsuoka et al. [14] studied the effect of the flexibility of an articulated robot on an end milling operation. Yu et al. [15] established the rigid and flexible dynamic equations for a polishing machine tool. This study calculated the influence of flexibility of each leg on the position of the moving platform. Plosa and Wojciech [16] presented mathematical and finite element models of beam-like links with bending and torsional flexibility. Zhang et al. [17] presented the critical issues and methodologies to improve robotic machining performance with flexible industrial robots. They developed a stiffness model and real-time deformation compensation was developed to control material removal rate (MRR). After the compensation, the surface error of machining a foundry cylinder head was improved from 0.9 mm to 0.3 mm.

However, current industrial robots are still too rigid and too big and might not be able to carry on machining tasks in narrow cavities where an endoscope could fit. Moreover, most industrial robot arms are still too heavy for portable applications, while an endoscopic tool could be carried with in a suitcase. Therefore, to enable an endoscopic tool with machining capability is worth study, which is a major topic of this paper.

1.4 Research Issues and Thesis Organization

1.4.1 Characterize static endoscopic tool

In the hypothesized grinding operation, the endoscopic bending section guides and supports the grinding tool, and the pose of the flexible tool will vary with the applied machining force. The grinding position and angle could be known and adjusted in real-time if we could “sense” the bending section by the result of pose estimation. Moreover, the pose and force are inextricably

coupled in this system. The knowledge of the pose and force are critical for the machining condition and material removal. The rigidity and deflection of the endoscope bending section are also valuable.

In chapter 2, static models that enable the pose and force sensing ability are described and models' accuracy are evaluated. An endoscope is taken apart and its inner mechanical structure is studied. Sensors are installed onto the endoscope and geometric model is build to study the kinetic characteristics of the bending section. The rigidity and deflection of the bending section are also studied by applying external force on to it.

1.4.2 Characterize dynamic stability of endoscopic tool

Because the bending section and base are non-rigid, chatter and dynamic stability can significantly affect the machining efficiency and MRR. The goal is to identify the dynamic response of the endoscopic tool and evaluate its dynamic stability. Once the dynamic stability map is built, grinding chatter and vibration can be avoided, minimized, or accounted for.

Chapter 3 presents a study of the endoscopic tool dynamics. A dynamic model is built to find out the fundamental frequency of the endoscopic machining system. Regenerative chatter theory is applied to portray the stability lobe diagram and the major cause of vibration is determined. A real time chatter detection method is proposed to help avoid unfavorable vibration during machining.

1.4.3 Quantify material removal rate of endoscopic machining

The ultimate goal of this research is the estimation and control of material removal by a flexible machining tool. If successful, material removal could be precisely controlled during machining process. In non-invasive machining tasks, for example, grinding out cracks on the jet engine turbine blade, it is important for engineers to know the amount of material removal and make sure the blades are still well balanced.

In Chapter 4, a MRR model is created based on the results of the static and dynamic studies. The material removal of a flexible machining experiment is estimated by this model and measured by the difference in mass of the workpiece. The error estimation and machining accuracy are discussed. By analytically modeling the chatter energy and power transmission overhead, the composition of grinding energy is determined. By empirically calibrating model parameters, the specific energy of endoscopic grinding tool is related to the material removal in the proposed

model. The repeatability and accuracy of the model are validated by endoscopic material removal experiments.

1.4.4 Conclusions and future work

The final chapter presents the overall conclusions, contributions, and future directions of this research. The endoscopic machining tool is proved a feasible means to conduct (force critical) machining tasks. MRR model is found to have reasonable prediction accuracy in endoscopic grinding experiments and chatter is found out not to be the primary contributor to the capability limitations. Methods to increase the accuracy of pose and force estimation are proposed and potential ways to achieve better MRR prediction accuracy is discussed as well.

Chapter 2

Static Modeling: Pose Estimation

2.1 Introduction

The major technical challenges of this research are methods for measurement and estimation of amount of material removed. In this study material is removed by grinding, in which it is assumed that the tool removes material on its lateral surface and from lateral forces. The material removal in a grinding process depends on tool rotational speed, contact force and contact area, the last two of which are addressed in this chapter. The pose (position and orientation) of the tool are important data for the area, mechanics, and geometry of the contact between the tool and workpiece. It will be shown that the pose and force data are coupled and whether predicted and/or measured, could reveal information about the contact area, machining condition, and material removal. Currently, no commercial model of endoscopes can sense and measure these quantities.

Inside the endoscope, there are metal mesh components protecting conduits for video signal, lighting source, air suction, water injection and biopsy tools. On the tip of the bending section, there is a camera channel providing a video signal for visual navigation and inspection. The bending section comprises pin articulated steel links (Ring in Figure 2.1) driven by two control knobs on the control handle through four steel cables. The steel driving cables are the key for the static study. The displacement of the driving cable is directly related to the bending angle of the bending section, while the tensile driving force on the cable is directly reflecting the external force exerted on the bending section. The external force will deflect the flexible bending section considerably from its original pose. If the displacement and tensile force of the driving cable is acquired, and their coupling relationship is known, the position and orientation of the bending section can be estimated.

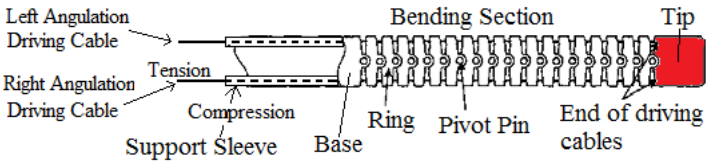

Figure 2.1. Endoscope bending section

This research aims to create an endoscope with position sensing and force measurement capabilities. The endoscope in this study was instrumented with an LVDT (Linear Variable Differential Transformer) sensor and a load cell to measure the displacement and the tensile force exerted on the driving cable, respectively.

In this chapter the method for measuring the true position, orientation and endoscopic force is explained. Then two models for pose (position and orientation) estimation and endoscopic force prediction are described. One is a geometric model, which is created to estimate the position and orientation of the endoscope in force free condition. The other is a force prediction model, which is built to predict endoscope position, orientation and force in forced condition. Experiments were setup to measure the true position, true orientation and external force of the endoscope for validation of the geometric model and force prediction model. Finally, the accuracy of the models is evaluated. This is the first step to achieving the ultimate goal of performing a precise endoscopic machining operation while removing a known amount of material from the workpiece.

2.2 Literature Review

Ikuta et al. [18] designed and developed a wire-driven 9 degree-of-freedom manipulator with 10 mm diameter for minimally invasive surgery called “Hyper Finger”. A special mechanism by Hirose and Chu [19] was used to address the drive wire elongation issue. However, force, torque and load capacity of this manipulator was not measured but only qualitatively described as “enough.” Hirose and Fukushima [20] introduced a string-driven and snake-like robotic design paradigm for search and rescue tasks. Bionic structures such as snake and spirochete were used in robotic locomotion design. Degani et al. [21] developed an minimally invasive surgical robot using on a novel two-concentric snakes mechanism. With a 12 mm in outer diameter and 300 mm in total length snake-like body, this robot is able to withstand 1 N to 5 N loads depending on the direction of the load and configuration of the robot. Mosse et al. [22] invented a device for measuring the force and torque exerted on the shaft of an endoscope. In this case, the endoscopist could be aware

of the thrust force and reduce the risk of perforating the organ during colonoscopy. These studies set the ground work for the current research, but the method for force and pose estimation have not been addressed in the literature, and becomes a major goal of this research.

2.3 Model Workflow

The pose and force are inextricably linked, i.e., the model couples them. Initially the pose model is formulated with force free boundary condition ($F_{ext} = 0$), where F_{ext} is external force, for simplicity. Then, external force ($F_{ext} \neq 0$) boundary condition is added for a more comprehensive model.

Figure 2.2 shows the work flow of position orientation estimation and force prediction. First, the LVDT sensor and the load cell have been carefully calibrated and compensated for non-linearity, shown in Eq. 2.3.1. Variable V_1 is the output voltage of the LVDT sensor in volt and V_2 is the load cell output in mV. Secondly, a real-time readout δ_{LVDT}, which is displacement measured by the LVDT sensor, was input to a Geometric Model G(δ_{LVDT}), shown in Eq. 2.3.2, to calculate force free position (X_{free}, Y_{free}) and orientation θ_{free} $(\angle EAR)$. Then, these calculated values plus a read-out F_{cell}, which is force in Newton from the load cell were applied to a Force Prediction Model, shown as functions η, κ, and λ in Eqs. 2.3.3 to 2.3.6, to obtain the forced position, orientation and predicted force:

$$\begin{cases} \delta_{LVDT} = 0.2483{V_1}^2 + 4.080V_1 - 0.0597 \\ F_{cell} = 1.1700V_2 - 0.5740 \end{cases} \tag{2.3.1}$$

$$(X_{free}, Y_{free}, Z_{free}) = G(\delta_{LVDT}) \tag{2.3.2}$$

$$\begin{cases} (X_{est}, Y_{est}) = (X_{free} + \Delta x, Y_{free} + \Delta y) \\ (\Delta x, \Delta y) = \eta(F_{ext}) \\ \text{Specially: } (0,0) = \eta(0) \end{cases} \tag{2.3.3}$$

$$\begin{cases} \theta_{est} = \theta_{free} + \Delta\theta \\ \Delta\theta = \kappa(F_{ext}) \\ \text{Specially: } 0 = \kappa(0) \end{cases} \tag{2.3.4}$$

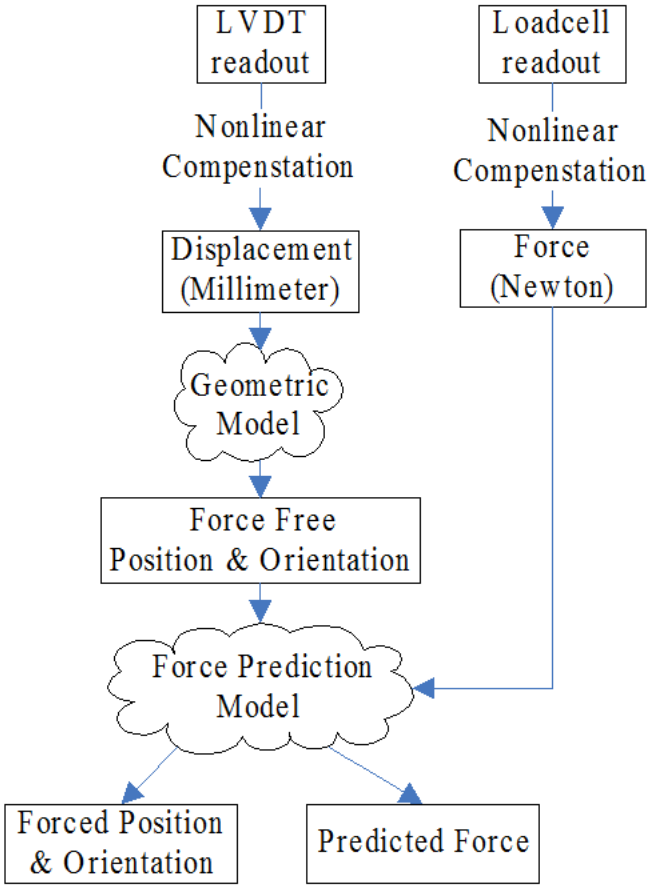

Figure 2.2. Work flow of pose estimation and force detection

$$\begin{cases} F_{cell} = F_{int} & F_{ext} = 0 \\ F_{cell} = \lambda(F_{ext}) + F_{int} & F_{ext} \neq 0 \end{cases} \tag{2.3.5}$$

$$F_{est} = F_{ext} = \lambda^{-1}(F_{cell} - F_{int}) \tag{2.3.6}$$

$$F_{int} \Leftrightarrow \mathbb{R}(\delta_{LVDT}) \tag{2.3.7}$$

where F_{int} is the intrinsic force on driving cable (see Figure 2.1) to bend the bending section and F_{int} has a unique mapping to δ_{LVDT}, as shown in Eq. 2.3.7, which is only decided by the intrinsic properties of the endoscope. In force free boundary condition, F_{int} should equal F_{cell}.

If subjected to force, F_{cell} should be a function of external force F_{ext} plus F_{int}, shown in Eq. 2.3.5. The frictional force can be calibrated within F_{int} and is not listed separately in this model.

2.4 Geometric Model: Pose Estimation in Force Free Condition

The geometric model has been abstractly described by Eq. 2.3.2, which has one input variable δ_{LVDT} and three outputs (X_{free}, Y_{free}) and θ_{free}. In detail, it comprises three governing equations as shown in Eq. 2.4.1:

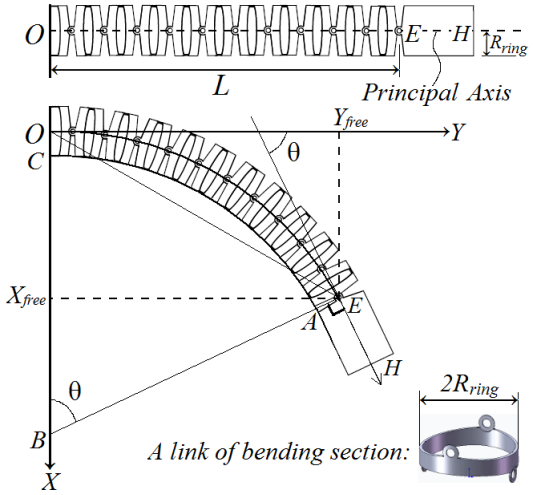

Figure 2.3. Pose estimation in geometric model

$$\begin{cases} X_{free} = 2R \times \sin(\dfrac{\theta_{free}}{2}) \times \cos(\dfrac{\pi}{2} - \dfrac{\theta_{free}}{2}) \\ Y_{free} = 2R \times \sin(\dfrac{\theta_{free}}{2}) \times \sin(\dfrac{\pi}{2} - \dfrac{\theta_{free}}{2}) \\ \theta_{free} = \dfrac{\delta_{LVDT}}{R_{ring}} \qquad (R_{ring} = 5.766mm) \end{cases} \tag{2.4.1}$$

$$\begin{cases} \dfrac{L}{R} = \theta \\ \\ \dfrac{L - \delta_{LVDT}}{R - R_{ring}} = \theta \end{cases} \Rightarrow \theta = \frac{\theta_{LVDT}}{R_{ring}} \in [0^0, 160^0] \tag{2.4.2}$$

In force free condition, it is assumed that the principal axis of bending section OE will always be an arc on a circle [23]. In Figure 2.3, the principal axis is $|OE|$ or $\overset{\frown}{OE}$, which has a constant length L. Variable R is radius of the arc formed by principal axis, which is $|BE|$ or $|BO|$.

R_{ring} is the radius of each link of the bending section, which is $|OC|$ or $|AE|$. Here R_{ring} is also a constant 5.766 mm.

Note that the tip is defined as point E, which is the last joint of bending section and the orientation angle θ is defined as the angle between Y-axis and vector $\overrightarrow{EH}$, which is the tangential direction of $\overset{\frown}{OE}$ at point E, as shown in Figure 2.3. Lastly, the accuracy of the geometric model in force free condition will be evaluated in the experiment result section.

2.5 Geometric model: Pose estimation with forced boundary condition

The bending section was modeled with equal length links for accurate prediction of the pose under forced boundary conditions, as presented in subsection 2.5.1. Then, the force on the driving cable was characterized and calibrated to the external force in subsection 2.5.2.

2.5.1 Pose Estimation with Force Constraints

The behavior of bending section can be divided into two superposition stages. First, the bending section bends freely to a certain position (X_{free}, Y_{free}) with θ_{free}. Second, an external force F_{ext} exerts on the bending section to generate the deflection $(\Delta x, \Delta y)$ and $\Delta\theta$. In this model, the predicted force F_{est} of F_{ext} is assumed to be a lateral force exerted on the distal point H of bending section and perpendicular vector $\overrightarrow{EH}$, as shown in figures 2.3 and 2.7.

The bending section is modeled as ten links ($Link_1$ to $Link_{10}$) articulated with revolute joints, which are moving within a 2D planar work space. As shown in Figure 2.4, each link has the same length of 8.20 mm. At the first stage, the revolute joints were set to their initial angle θ_i ($i = 1$, 2, 3 to N, $N = 10$), while all joints were subjected to zero external force, having zero potential energy. Then an external force, F_{ext}, was applied to the end of the last link. Each joint acts as a helix spring with Hook constant K_i (Fig. 2.4).

In the force prediction model, there are two constraints. The first is an equilibrium constraint – each revolute joint, J_i , will be rotated by an angle $\Delta\theta_i$ to generate a reaction torque τ_i , as shown in equation 2.5.1. Variable d_i is the moment of joint J_i , as shown in Figure 2.4.

$$\tau = K_i \cdot \Delta\theta_i = F_{ext} \cdot d_i \tag{2.5.1}$$

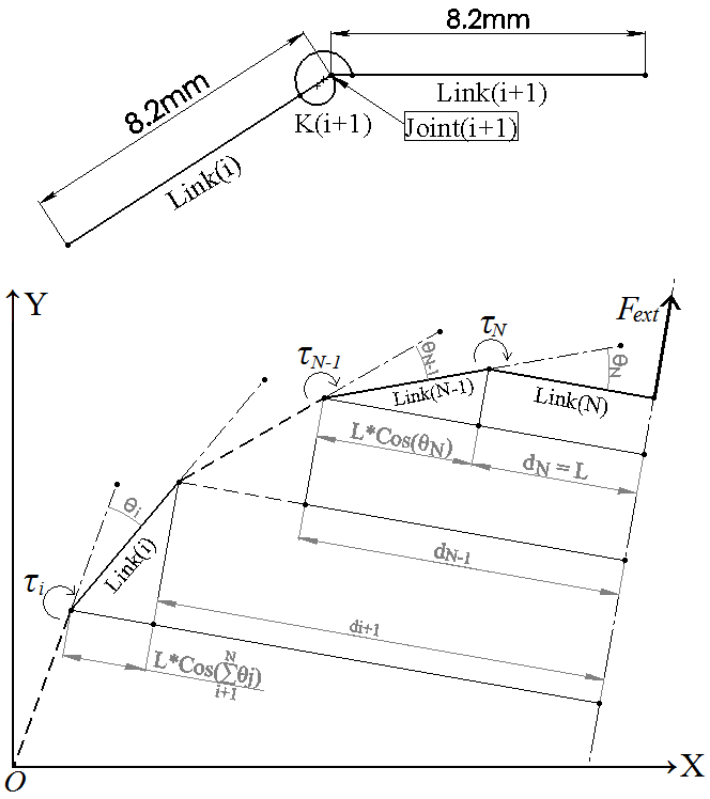

Figure 2.4. Pose estimation in force prediction model (assume F_{ext} is given)

The second is cable length constraint. Since the control knob should be locked after turning the bending section to a certain position, the driving cable will stay in position no matter how large an external force F_{ext} is exerted on the bending section. In this case, the length of $\overset{\frown}{CA}$ should be a constant as long as the control knob is locked, neglecting cable sliding and stretching. The sum of joint angles $\theta_{total} = \sum_{i=1}^{N} \theta_i$ will be nearly a constant if δ_{LVDT} does not change.

In the force free condition, each θ_i is assumed to share the same division of total $\frac{\theta_{total}}{N} (N = 10)$, hence the bending section can be an arc of a circle. In forced condition, θ_{total} though not different, will be unevenly redistributed to each θ_i according to joint torque τ_i . Therefore, the force prediction model can be described with Eqs. 2.5.2 to 2.5.8.

For the last joint J_N $(N = 10)$:

$$d_N = L \qquad (L = 8.2mm) \tag{2.5.2}$$

$$\Delta\theta_N = \frac{\tau_N}{K_N} = \frac{F_{ext} \cdot d_N}{K} \qquad (\text{Let } K_N = K) \tag{2.5.3}$$

$$\Delta\theta'_N = \Delta\theta_N - \left(\sum_{j=1}^{N\text{-}1} \dot{\Psi}_{N_j} \cdot \Delta\theta_j \right) \tag{2.5.4}$$

For joint J_i:

$$d_i = d_{i+1} + L\cos\left[\sum_{j=1+1}^{N} (\theta_j - \Delta\theta'_j) \right] \tag{2.5.5}$$

$$\Delta\theta_i = \frac{F_{ext}}{K_i} = \frac{F_{ext} \cdot d_i}{K} \tag{2.5.6}$$

$$\Delta\theta'_i = \Delta\theta_i - \left(\sum_{j=1}^{i\text{-}1} \dot{\Psi}_{ij} \cdot \Delta\theta_j + \sum_{j=i+1}^{N} \dot{\Psi}_{ij} \cdot \Delta\theta_j \right) \tag{2.5.7}$$

$$\sum_{i=1}^{j\text{-}1} \dot{\Psi}_{ij} + \sum_{i=j+1}^{N} \dot{\Psi}_{ij} = 1 \qquad (j \in [1..N]) \tag{2.5.8}$$

Note that $\dot{\Psi}_{ij} \quad (i, j \in [1..N], i \neq j)$ are weight factors controlling the redistribution of θ_{total} .

$$\begin{cases} X_{est} = \sum_{i=2}^{N} \left[L\sin\left(\sum_{j=1}^{i} \frac{\theta_{free}}{N} - \Delta\theta'_j \right) \right] \\ Y_{est} = L + \sum_{i=2}^{N} \left[L\cos\left(\sum_{j=1}^{i} \frac{\theta_{free}}{N} - \Delta\theta'_j \right) \right] \\ \theta_{est} = \theta_{free} - \sum_{i=1}^{N} \Delta\theta'_i \end{cases} \tag{2.5.9}$$

Equation 2.5.9 governs final outputs of force prediction model, which are estimated position (X_{est}, Y_{est}) and orientation θ_{est} in forced condition.

2.5.2 Characterization of intrinsic and external force on driving cable

Since the bending section of endoscope has a skeleton structure and all of its links are articulated by passive joints which can rotate freely, F_{int} should be zero when the bending section stays still in an arbitrary position, if neglecting friction, gravity and external force. In fact, F_{int} is not zero because there are several interior channels residing in bending section, including one channel for biopsy tools, two light fiber channels, one camera channel and channels for air suction and water injection. Since all the channels are made from or coated by plastic pipes, F_{int} is actually a pipe bending force. For accuracy of model evaluation, all the pipes are cut off and removed except the biopsy pipe (outer diameter is 4.5 mm, wall thickness is 0.5 mm), which is left for holding the transmission shaft for machining.

Figure 2.5 shows the last two joints of bending section in equilibrium. F_{ext} is external force perpendicular to EH. $(F_{cell} - F_{int})$ is reaction force on the driving cable. For link EH, torques generated by external force and reaction force should balance each other, as shown in Eq. 2.5.10.

$$(F_{cell} - F_{int}) \times 5.77 = F_{ext} \times 16.03 \tag{2.5.10}$$

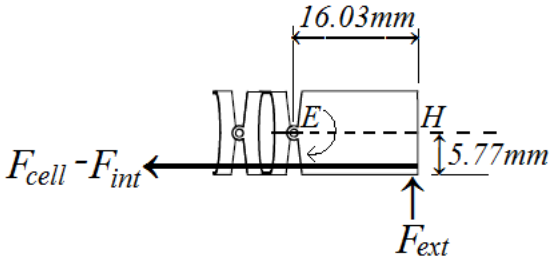

Figure 2.5. Force prediction in equilibrium state
(F_{ext} is unkown)

Therefore, the estimated force can be found as in Eq. 2.5.11, and the relationship between int F_{int} and $\mathbb{R}(\delta_{LVDT})$ can be decided using empirical data, shown in Figure 2.6.

$$F_{est} = \frac{(F_{cell} - F_{int}) \times 5.77}{16.03} = \frac{F_{cell} - (\delta_{LVDT})}{2.778} \tag{2.5.11}$$

The relationship of F_{int} and δ_{LVDT} is given by Eq. 2.5.12.

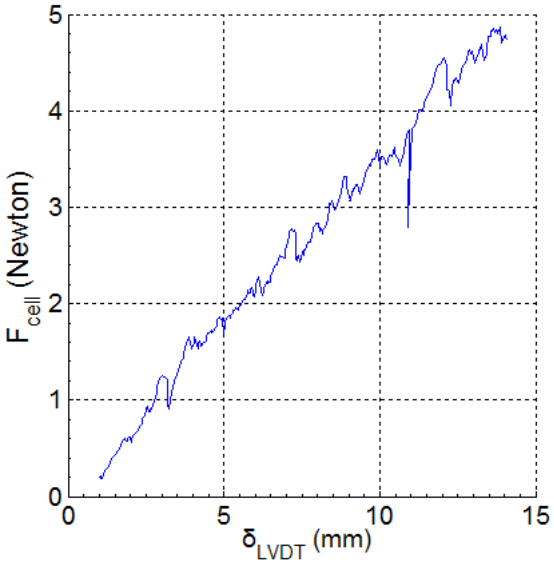

Figure 2.6. F_{cell} and δ_{LVDT} in force free condition

$$\begin{cases} F_{cell} = F_{int} = 0.3531\delta_{LVDT} - 0.02672 \\ F_{ext} = 0 \qquad \text{(Froce free)} \end{cases} \tag{2.5.12}$$

Combining Eqs. 2.5.11 and 2.5.12, F_{ext} is estimated by Eq. 2.5.13.

$$F_{ext} \approx F_{est} = \frac{F_{cell} - 0.3531\delta_{LVDT} + 0.02672}{2.788} \tag{2.5.13}$$

2.6 Experiment Setup for Pose and Force Measurement

2.6.1 LVDT and Load Cell Measurement Setup on Endoscope

A PENTAX ES-3801 endoscope was partially disassembled and then reassembled with a LVDT displacement sensor and a load cell, as shown in Figure 2.7. The control handle and the base of the bending section are rigidly fixed with screws. Estimated position and orientation are derived only by the readouts of the LVDT sensor and the load cell using analysis approach. At the same time, the true X-Y position and orientation of the tip are acquired in real-time using a computer vision approach called object tracking [24, 25]. The true X-Y position data is used to help analyze the behavior of endoscope bending section and to verify the estimated position and orientation.

In this study only two dimensional movement will be considered without any loss of generality in 2D analysis. In Figure 2.7, the position of the tip of endoscope (point E) is measured in reference frame $\{O\}$, the origin of $\{O\}$ is coincident with the base (point B) of bending section, where it is supported by a balloon during machining. In the experiment, the base of bending section is rigidly fixed on metal brackets for accuracy and simplicity.

Since the tip of the bending section is driven by the control knob through four steel cables that move up/down and left/right, the pose and forces of endoscope tip is a function of the displacement and tensile force of the driven cables as shown in equation 2.6.1:

$$\begin{cases} (x, y, \theta_{2D}, f_{2D}) = F(\delta_1, f_1) & \text{in 2D} \\ (x, y, z, \theta_{3D}, f_{3D}) = F(\delta_1, \delta_2, f_1, f_2) & \text{in 3D} \end{cases} \tag{2.6.1}$$

where x, y, and z are the Cartesian position of the tip of endoscope and θ is tip angle represented in reference frame $\{O\}$, θ_1, θ_2 are displacements of driving cables measured by LVDT sensor, f_1 and f_2 are tensile forces on driving cables measured by the load cell. The position of endoscope tip with regard to the base of bending section is only a function of the displacement of driving cable and external force exerted on it.

For simplicity, in grinding process, the external forces are assumed always perpendicular to the axis of the tip. Note that due to the structure of bending section, the vertical (up/down) and horizontal (left/right) movement of endoscope tip is not independent, and their coupling relationship was studied by Lipkin and Munnae [23] using robotics approach.

2.6.2 Pose Validation System

It is important to accurately measure the position in any position estimation task externally, hereafter termed the true position, for validation of the estimation method. In the experiments, the 2D true X-Y position and orientation of the endoscope tip was acquired using object tracking, in which markers were attached at crucial points on the endoscope and tracked with customized computer software, as shown in Figure 2.8. The steps in the true position acquisition are detailed below:

1. A camera was placed above and carefully aligned with the bending sections work plane to get the top view of the whole 2D planar work space of the tip.
2. Four red markers were attached to the base (B), the tip (H and E) of bending section and another reference point (R), as shown in Figures 2.8 and 2.9.

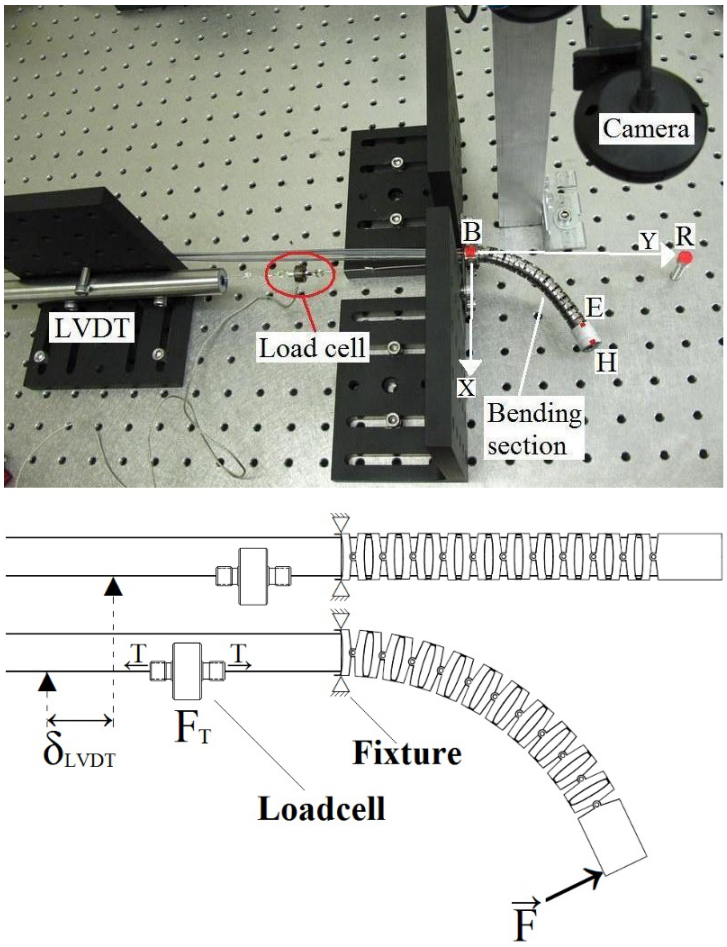

Figure 2.7. Experimental setup of LVDT sensor and load cell (top view)

Note: δ_{LVDT} is displacement measured by LVDT sensor (Macro Sensors SE750-2000). F_T is tensile force measured by load cell (Delta Metrics XLUS88). Data acquisition device is National Instrument PCI-6221.

3. In MATLAB, input video frames were converted to Red-Green-Blue color space from original YUY2 color space and then passed through a color filter to extract all red color objects.

4. The color video frames were transformed into black and white frames by an appropriate threshold.

5. An object tracking tool called Blob Analysis was applied to find out the pixel locations and centroids of all blobs in video.

6. A calculation program turned pixel locations and centroid values into true X-Y positions and orientation angle and rendered these values to original video signal for display.

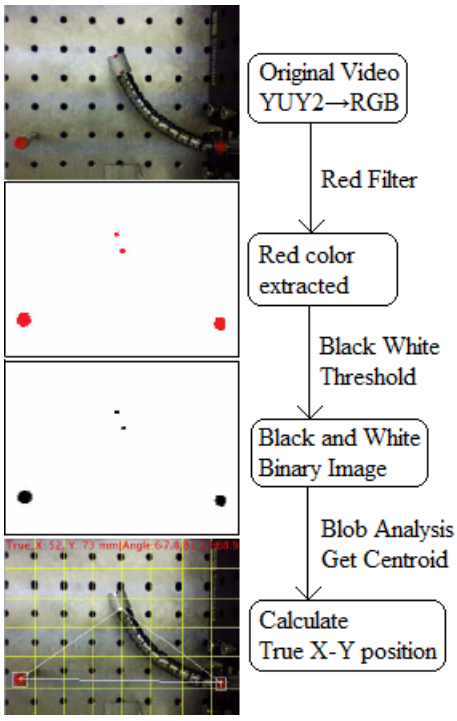

Figure 2.8. Camera output and markers of object tracking method

Figure 2.9 also shows trigonometric calculation for true positions and orientation from pixel positions. $R(H_R, V_R)$, $E(H_E, V_E)$, $H(H_H, V_H)$ and $B(H_B, V_B)$ are the 2D centroids of reference point, bending section tip and base in the pixel coordinate system. The origin, point O, is coincident with base point, B. The direction of vector $\overrightarrow{BR}$ was set as $True\_Y$ direction of reference frame $\{O\}$, and $True\_X$ direction perpendicular to the Y direction. In this experiment, the endoscope is assumed to work in plane XOY.

Then the true position of $E(True\_X, True\_Y)$ is represented as:

$$\cos(\angle R) = \frac{|BR|^2 + |RE|^2 - |BE|^2}{2(|BR| \times |RE|))} \tag{2.6.2}$$

$$|Y| = |BR| - [\cos(\angle R) \times |RE|] \tag{2.6.3}$$

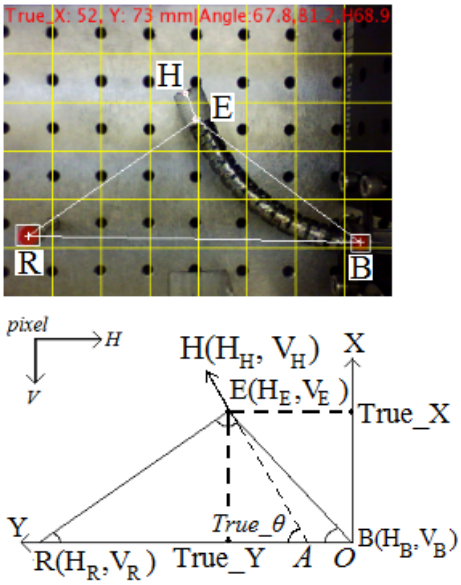

Figure 2.9. True X-Y position and orientation of bending section tip
(X: 52 mm, Y: 73 mm, θ: 67.8 degree)

$$|X| = \sqrt{|RE|^2 - (|BR| - |Y|)^2} \tag{2.6.4}$$

$$|True\_X| = |X| \times (\frac{|True\_BR|}{|BR|}) \tag{2.6.5}$$

$$|True\_Y| = |Y| \times (\frac{|True\_BR|}{|BR|}) \tag{2.6.6}$$

$$True\_\theta = \angle EAR \tag{2.6.7}$$

Note that $|True\_BR|$ in Eq. 2.6.5 is a constant distance between base B and reference point R, and in this experiment, it is 145.2 mm. Moreover, although the camera is carefully aligned with the work plane of endoscope, there is inevitable error in optical channel due to camera deployment, video resolution (QVGA), lenses distortion and perspective distortion. However, the worst case error is less than ± 2 mm and average error is limited to ± 1 mm of true position acquisition. The resolution of orientation angle θ is 0.1 degree, and the average error is within ± 1 degree. Figure 2.10 shows the work space of the tip of bending section in force free boundary condition,

which is generated by tracing the tip (here is midpoint of $|HE|$) moving back and forth 10 times. It demonstrates high repeatability of the measurement result.

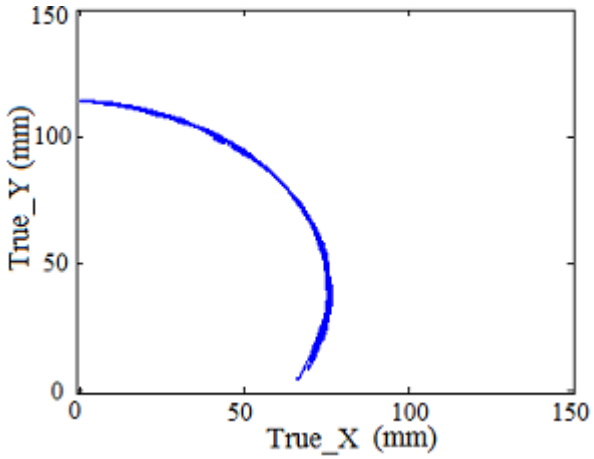

Figure 2.10. Work space of the tip in force free boundary condition
(Measured 10 times, standard deviation $\delta_x \leq 1$ mm)

2.6.3 Force Validation

To evaluate force error, an external force that is normal to the bending section tip is exerted on the bending section tip by a spring scale (resolution $0.1N$) and F_{ext} is read from the scale. F_{est} is estimated by using Eq.2.5.13, which depends only on F_{cell} and δ_{LVDT}. At the same time, F_{est} is plugged into Eq. 2.5.6 as F_{ext} to estimate forced position and orientation angle. Because the spring scale read out cannot be sampled by computer directly, force error evaluation experiment is done manually. The experiments are carried out three times to get an average result.

2.7 Experiment Results and Model Evaluation

2.7.1 Geometric Model Error: Force Free Boundary Condition

In the experiment the bending section of endoscope was moved slowly from its straight position to fully bended position while data points were sampled (belongs in setup/procedure). Figure 2.11 shows the trace of tip (Point E in Figure 2.9) of the bending section during the experiment. The solid line is the $(True\_X, True\_Y)$ acquired by video tracking. The dotted line is estimated tip

position (X_{free}, Y_{free}) by geometric model. Figure 2.12 shows the true orientation angle $True\_\theta$ and estimated angle θ_{free}.

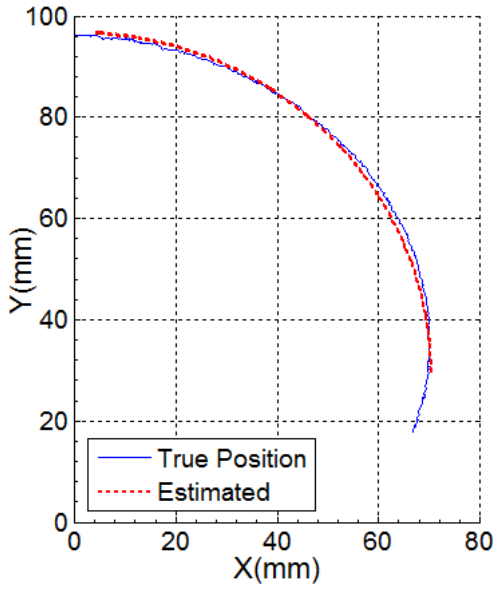

Figure 2.11. True and estimated position trace

The quantified error is defined as: X_{error}, Y_{error}, Position Error (P_{error}) and Orientation Angle Error (A_{error}) in Eqs. 2.7.1 to 2.7.3.

$$\begin{cases} X_{error} = X_{est} - True\_X \\ Y_{error} = Y_{est} - Ture\_Y \end{cases} \tag{2.7.1}$$

$$P_{error} = \sqrt{(X_{est} - True\_X)^2 + (Y_{est} - True\_Y)^2} \tag{2.7.2}$$

$$A_{error} = \theta_{est} - True\_\theta \tag{2.7.3}$$

Figures 2.13 and 2.14 show the estimated position error on X direction and Y direction respectively. At the very beginning, the X_{error} is much larger than Y_{error} because the tip of bending section started to move from its singularity point, which means the tip moves much faster in X direction than it moves in Y direction per unit δ_{LVDT}.

Figures 2.15 and 2.16 describe the position error and angle error in detail. These results show that as bending section bends more (as Y position decreases), the errors become larger. That is

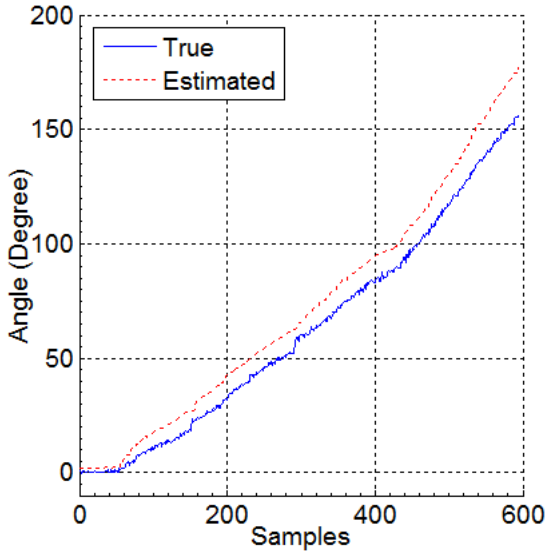

Figure 2.12. True and estimated orientation angle

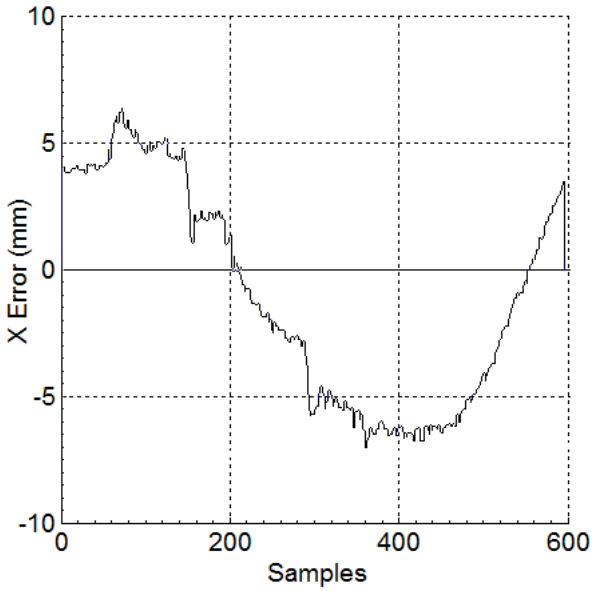

Figure 2.13. Estimated error in X direction

because when bending section bends, the reaction force of interior plastic pipe will push against the bending section, which makes it no longer a perfect arc on a circle. Therefore, the geometric model loses its accuracy once external force becomes significant. The force prediction model minimizes and compensates estimated errors by modeling such a reaction force as an external force.

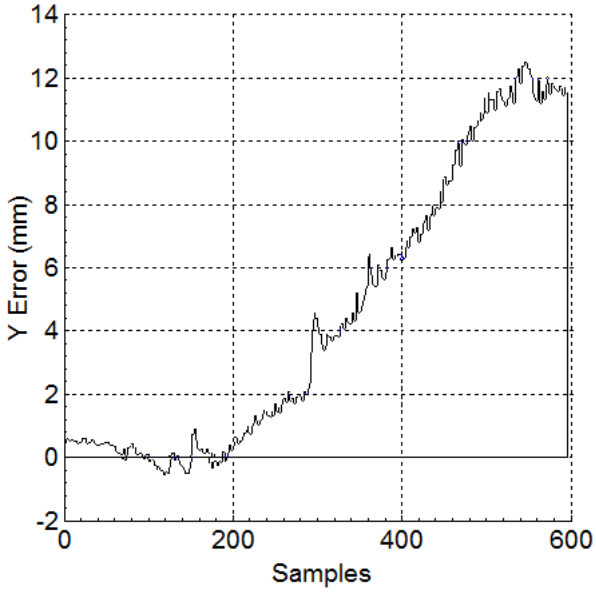

Figure 2.14. Estimated error in Y direction

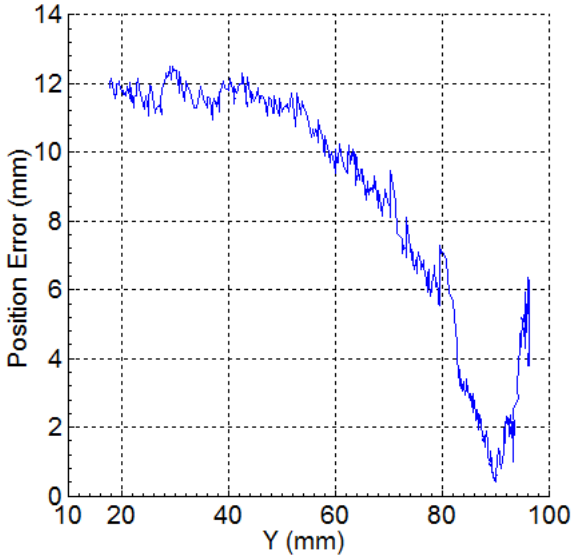

Figure 2.15. Position estimation error with regard to Y position

2.7.2 Static Force Model Error: Forced Boundary Condition

Pose Estimation Errors

In the force prediction model, the interior reaction force generated by the plastic pipe as the internal tool channel could be modeled as a pseudo external force perpendicular to the tip of

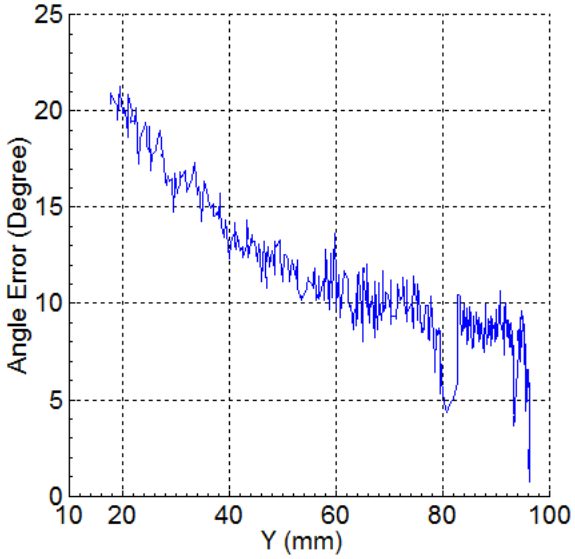

Figure 2.16. Orientation angle estimation error with regard to Y position

the bending section. In this case, the F_{int} is compensated and position and orientation estimation becomes more accurate.

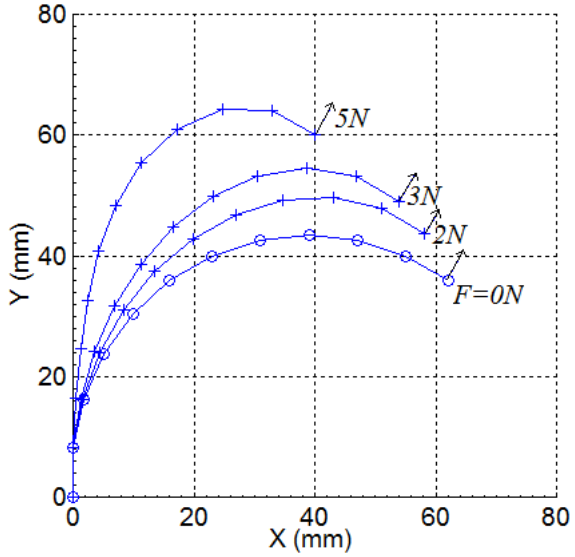

Figure 2.17. Force prediction model outputs

(θ_{free} = 120^o, joints Hook's constant K=10, external force F=[0,2,3 and 5 N] perpendicular to tip)

Figure 2.17 shows estimated results under different external force conditions. It gives an intuitive feeling of how the force prediction model works. The joint number was set $J = 10$, link

length $L = 8.2$ mm and the initial angle of bending section was set as $\theta_{free} = 120^o$ in this example. Hook constant, K_i , of each joint was set to 10. The weight factor was set $\Psi_{ij} = \frac{1}{N-1} \quad (i, j \in [1..N], i \neq j, N = 10)$ for all ten joints. The external force, F_{ext}, was set to 0, 2, 3, and $5N$ respectively and the simulation was run to get compensated orientation angle and tip position. Each circle or cross in Figure 2.17 represents a passive joint.

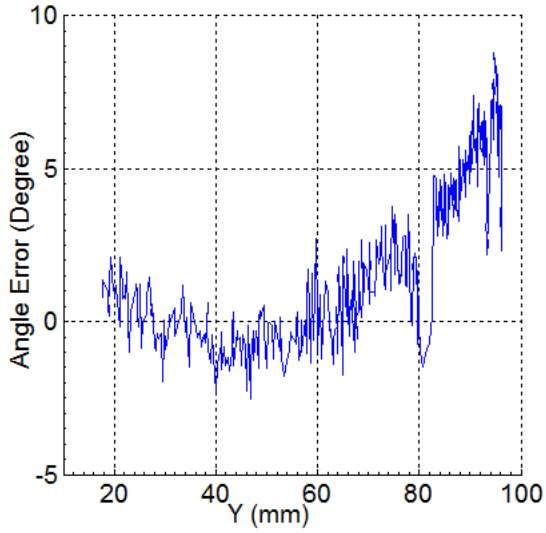

Figure 2.18. Orientation angles estimation error with regard to Y position
(Internal force F_{int} Compensated)

Figures 2.18 and 2.19 show the orientation angle error and position error of force predicted model. By compensating bending section deflection caused by internal driving force, the estimation accuracy is improved by at least 100% for all positions. Without compensation, the average angle error is above 15 degrees and average position error is larger than 8 mm. In contrast, the compensated average errors are less than 5 degrees and 4 mm. Moreover, these results are achieved by simply setting all weight factors $\dot{\Psi}_{ij}$ to a constant $\frac{1}{N-1}$. If the weight factors are optimized for each joint, the results should be more accurate.

Due to the experimental setup limitation, it is difficult to keep F_{ext} as a constant and evaluate position and orientation errors in whole workspace under a certain forced condition. However, in the following experiment, position and orientation errors are evaluated at discrete points under different forced conditions.

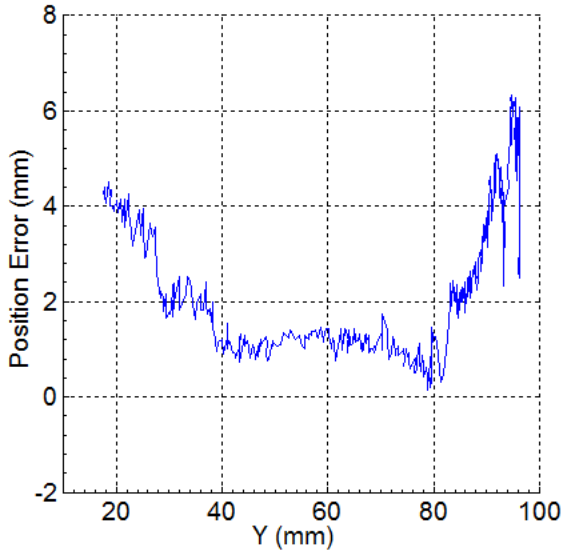

Figure 2.19. Position estimation error with regard to Y position
(Internal force F_{int} compensated)

Force Prediction Errors

Force prediction error is defined as 2.7.4

$$F_{error} = F_{est} - F_{ext} \tag{2.7.4}$$

Table 2.1 shows the force error measured under different position-force combinations. In most conditions, the estimated force error is less than $0.5N$. Note that when bending angle $\theta_{free} < 90^o$, the bending section cannot bear much external force, hence the combinations with smaller bending angle are not evaluated.

Table 2.2 shows the position and orientation error in different forced conditions. Note that when external force is less than 4 N, the estimation error is low. When external force exceeds 5 N, the bending section buckles in vertical direction. That means the principal axis of bending section is not in a plane any more and estimation errors increase rapidly.

Table 2.1. Force prediction error

F_{ext}	F_{error} *(Newton)*			
	$\theta_{free} = 90^o$	120^o	140^o	160^o
$0N$	-0.537	-0.605	-0.650	-0.361
$1N$	-0.036	-0.457	-0.484	-0.393
$2N$	0.307	-0.222	-0.433	-0.317
$3N$	0.592	0.078	-0.501	-0.445
$4N$	n/a	n/a	-0.424	-0.150
$5N$	n/a	n/a	-0.017	-0.246
$6N$	n/a	n/a	n/a	-0.242

Table 2.2. Position and orientation error in forced boundary conditions

F_{ext}	$P_{error}(mm)$ / $A_{error}(degree)$			
	$\theta_{free} = 90^o$	120^o	140^o	160^o
$1N$	$1.2/2.1^o$	$1.1/0.8^o$	$2.5/3.3^o$	$4.1/3.5^o$
$2N$	$2.2/0.8^o$	$1.7/4.3^o$	$3.4/-0.8^o$	$3.2/-0.7^o$
$3N$	$2.7/5.5^o$	$2.5/6.0^o$	$4.9/5.5^o$	$6.3/5.8^o$
$4N$	n/a	n/a	$6.1/-8.5^o$	$5.9/-2.4^o$
$5N$	n/a	n/a	$7.7/-10.4^o$	$2.8/-10.2^o$
$6N$	n/a	n/a	n/a	$8.9/-15.6^o$

2.8 Conclusions

It is important to be able to estimate the position and force exerted onto the tip of an endoscope for a precise machining operation from a flexible base. In this research, the methods for measuring and estimating the position of the tip of the endoscope were developed and tested. The endoscope was instrumented with LVDT sensor and force sensor for measurement of the change in position and force of the driving cable, respectively. This measurement output could then be correlated to the X-Y position and orientation of the tip of the endoscope under different boundary conditions.

Two simple models were constructed to estimate the pose and force of the bending section based on its geometrical structure. The estimated outputs of the models were compared to the true position and orientation measured visually by a camera and force measured by a spring scale.

The overall accuracy of these two models was reasonable. The true accuracy of the whole experiment setup was limited by video tracking, which was about 1 mm. The accuracy of geometric model was influenced by reaction force generated by internal channels (plastic pipes) and was poor without internal force compensation (average angle error > 15 degrees, average position error > 8

mm). By considering the internal reaction force in the force prediction model, the compensated average position error and orientation error were improved to less than 4 mm and 5 degrees.

The average error of the force prediction is less than 0.5 N. The accuracy of position and orientation estimation in forced condition dropped as the external force exceeded 5 N because of bending section buckling in vertical direction. Better accuracy is needed for precise machining, but this possibly could be achieved by optimizing weight factors $\dot{\Psi}_{ij}$ and employing a better position tracking systems (like active infrared 3D tracking system with 0.1 mm accuracy).

Since the bending section was bent from 0 degree to only one direction (X positive direction) in every experiment and was always preloaded by F_{int} while it was bending, the driving cable hysteresis and joint backlash were compensated by the F_{int} calibration. The deformation error of the driving cable is much smaller comparing to other error factors, therefore it is negligible.

Since the later on MRR prediction result will depend on the pose and force estimation results, the ideal accuracies of pose and force estimation should be a fraction of 0.1 mm and 0.1 N respectively.

Chapter 3

Analysis of Vibration and Machining Dynamics

3.1 Introduction

Vibration in machining can be categorized as either independent of or caused by the material removal process. Independent vibration is called external vibration, such as transmitted vibration through a common foundation or vibration caused by a rotating spindle driving by defective gear teeth. Ways to control or eliminate independent vibration include better machine tool design, siting the machine properly and maintenance [26].

Internal vibration was classified by DeVries [26] into two subtypes: internally forced vibration and self-induced or chatter vibration a.k.a. self-excited vibration, regenerated vibration. Internally forced vibration occurs because of the chip making process. For example, in face milling, the periodic forces can excite a relative vibration between the machine tool and workpiece. Chatter occurs in the machining process that produces a new surface by removing material from a surface generated by a previous action. Undulation on the previously generated surface can cause vibrations to regenerate rather than die out.

Chatter is one of the most critical issue in machining process. Chatter will inevitable degrade surface finishing, dimension accuracy, tool life and even machine reliability[27]. Although chatter has been observed and studied in many different machining processes, such as milling[28], turning[29][30], and boring[31][32][33], it is more crucial in grinding, because it impairs two main objectives of grinding – high dimensional accuracy and better surface finish of workpiece ground[34]. Among these studies, researchers found ways to suppress chatter and the approach is stability analysis.

In non-rigid machining, the flexibility of the endoscopic tool renders stability to be an even more severe issue. Since chatter is an unwanted phenomenon in machining process, which could seriously degrade geometric accuracy and surface finish of workpieces and even damage machining tools, it should be always carefully avoided. Here, the word "chatter" is used as an equivalent to self-excited vibration. Although the presence of chatter could be observed and detected by experienced machine operators during the machining process or after, it is comparatively more difficult to be detected in an automatic manner. Only a few methods using acoustic emission (AE) could be found in a review of grinding chatter conducted by Inasaki et al. [34] in 2001. Govekar et al. [35] and Gradisek et al. [36] proposed two new methods for automatic chatter detection in grinding using a non-linear statistic called the coarse-grained information rate and an entropy indicator in 2002 and 2003, respectively. More recently, Wang and Liang [37] in 2009 presented a chatter detection method by statistically analyzing the wavelet transform modulus maxima, which is independent of process parameters and less susceptible to cutting condition changes. Al-Regib and Ni [38] in 2010 proposed a method of on-line machine-tool chatter detection by characterizing the significant transition in the cutting dynamics at the onset of chatter. Although all of these methods are quite valuable and inspiring, none of them are dedicated to nor verified effective for non-rigid machining. In this chapter, a dynamic model is proposed to study the stability of endoscopic grinding tool. An algorithm is built to detect the frequency and magnitude of chatter. Forced chatter suppression method is discussed.

3.2 Literature Review

In traditional rigid machining, chatter vibration and dynamic effects have been studied for more than 50 years. Internal forced vibration (also called forced vibration) is usually more straightforward and better understood [34] and self-excited vibration (regenerative chatter) is more complicated and considered the most significant source of machining chatter [39]. Regenerative chatter theory has been studied and applied in many machining processes to suppress vibration, such as milling [28][40], turning [29][30], drilling [41][42], and boring [31][32][33].

Regenerative chatter and dynamic effects of rigid grinding process has also been pervasively studied. Mathematical analytical models of conventional rigid grinding process could be found in many textbooks[27][26][43]. Snoeys and Brown [44] found out dominating parameters of chatter in grinding process by theoretical analysis. Wager et al. [45] analyzed the growth rates and decay rates of vibration in grinding process using a numerical approach. Steffens and Follinger [46]

proposed a more sophisticated mathematical model to analyze and simulate the dynamic effects in grinding process. As he stated, the single-degree-of-freedom mass-spring with viscous damping model is widely used to analyze forced vibrations and self-excited vibration. This simple model is most suitable for simple machinery and ideal structures and numerous masses, springs and damping elements connected together could be build to simulate complex structures. But in practice choosing the appropriate values for each element is difficult [46]. Tonshoff et al. [47] described a comprehensive model set of modeling and simulation of grinding process, which includes kinematic model, topography model, chip thickness model, energy model, force model, temperature and surface integrity model and surface roughness models. Gradisek et al. [36] proposed entropy and coarse-grained information rate (CIR) methods to detect early stage chatter in grinding process.

With the development of robotics, more and more industry robots have been involved in machining processes to substitute human labor force and traditional machinery [48][49]. Due to the structural configuration of serial-link robotic manipulators, they are much more flexible than traditional machinery, but also more vulnerable to forced vibration and regenerative chatter because of lower structural stiffness[17]. Researches have been conducted in chatter detecting, modeling and suppressing. Wang and Liang [37] proposed a statistical chatter detection method based on the study of discrete wavelet transform scheme and statistical analysis of wavelet transform modulus maxima. Zhang et al. [17] proposed a stiffness modeling method to real-time compensate manipulator's deformation in order to achieve higher productivity and better surface accuracy. Raibert and Craig [12] proposed hybrid control theory of robotic manipulator, which achieved stable and accurate control of force and position trajectories. Pan et al. [50] [51] proposed mode-coupling chatter theory to analysis and suppress chatter in robotic machining process. Besides, Matsuoka et al. [14] proposed a more accurate flexible end milling process by using small diameter end milling tool head and high speed spindle.

3.3 Dynamic Model

A dynamic model was built to study the vibration characteristics of the endoscopic tool. The model shown in figure 3.1 comprises two parts. The first part is the bending section with a fixed base B and a free tip A in 2D workspace, being modeled as a torsional spring (k_1) damper (c_1) located at the first rotational joint J_1 from B, and a moment of inertia, $I(m_1)$. The second part is a piece of aluminum workpiece installed on the dynamometer, which is modeled as a simple sping (k_2) mass (m_2) damper (c_2) model. The bending section is initially bent to a preload angle φ and

locked. Initially, the tool head, which is assumed to be coincident with point A, was pressed against the workpiece with a preload normal force F_p. The contacting force F is a linear combination of F_p and the sinusoidal grinding normal force modeled as $Asin(\omega t)$.

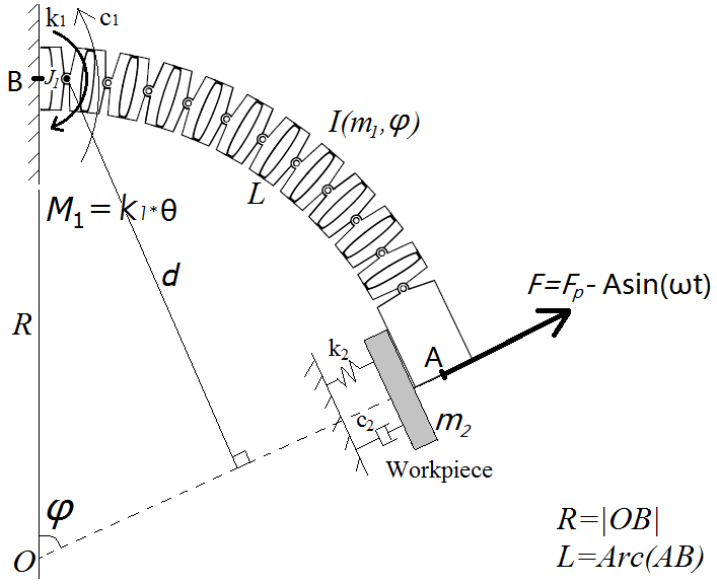

Figure 3.1. Dynamic model

$$\begin{cases} I(m_1)\ddot{\theta} + c_1\dot{\theta} + k_1\theta = F(t) \\ m_2\ddot{x} + c_2\dot{x} + k_2 x = F(t) \\ x = d \cdot tan(\theta) \approx d \cdot \theta \end{cases} \tag{3.3.1}$$

$$\begin{cases} \dfrac{\Theta(s)}{F(s)} = \dfrac{1}{IS^2 + c_1 S + k_1} \\ \dfrac{X(s)}{F(s)} = \dfrac{1}{m_2 d S^2 + c_2 S + k_2} \\ X(s) = d\Theta(s) \end{cases} \tag{3.3.2}$$

Equation 3.3.1 is the governing equation of the dynamic model. The values of constants and coefficients used in this model are shown in Table 3.1. It should be noted that the length of bending section is described by arc $\overset{\frown}{AB}$ in Figure 3.1 and the mass of inertia of the endoscopic tool ($\varphi = 90^o$) is calculated by equation 3.3.3. By taking a Laplace transform over equation 3.3.1, the dynamic model can be described using equation 3.3.2. Dynamic characteristics of the model

could be calculated by using pole-zero map function, impulse function and bode plot function in the Matlab, as shown in Figure 3.2.

Table 3.1. Constants and coefficients in dynamic model

Mass and Inertia	$m_1 = 10m_{Link}$	kg	6×10^{-2}
	m_2	kg	1.08
	$I(m_1, \varphi)$=$0.307m_1L^2$	kg · m²	1.528×10^{-4}
Bending Section Length	L	m	0.082
Spring Coefficient	k_1	N·m/rad	0.812
	k_2	N/m	4×10^{8}
Viscous Damping Coefficient	c_1	N·m·s/rad	0.005
	c_2	N·s/m	1000
Bending Angle	φ	rad (degree)	0.785 (90)
Moment Arm	d	meter	5.2×10^{-2}
Preload Normal Force	F_p	N	5
Machining Normal Force	A	N	2
$Asin(\omega t)$	ω	rad/s (Hz)	523.4 (83.3)
Natural Frequency	f_{n1}	Hz	≈ 13
	f_{n2}	Hz	≈ 3100

$$I = \sum_{i=1}^{10} m_{Link} \cdot d_i^2 = \frac{m_1}{10} \sum_{i=1}^{10} [2R \cdot sin(\frac{\varphi}{10} \cdot \frac{i}{2})]^2 \approx 0.307 m_1 L^2 \qquad (\varphi = \pi/2) \qquad (3.3.3)$$

The calculation of the natural frequency of the endoscopic tool and workpiece results in 13 Hz and 3.1 KHz, respectively. These results are not meant to be very accurate, but still reveal information that the endoscopic tool has a very low natural frequency in comparison with the workpiece. In other words, when the tool head is machining at 5,000 rpm spindle speed, which is 83.3 Hz, the induced sinusoidal machining normal force is more likely to generate significant vibration on the endoscopic tool than the workpiece. The amplitude of step response diagram in Figure 3.2 demonstrates that the vibration is mainly contributed by the endoscopic tool and the contribution of the workpiece could be neglected (10^{-9}).

3.4 Chatter Prediction Using Regenerative Chatter Theory and Stability Lobe Diagram

Tlusty [52] and Tobias [53, 54] conducted early studies of machining chatter prediction. They proposed that the boundary between a stable cut (chatter free) and an unstable cut (with chat-

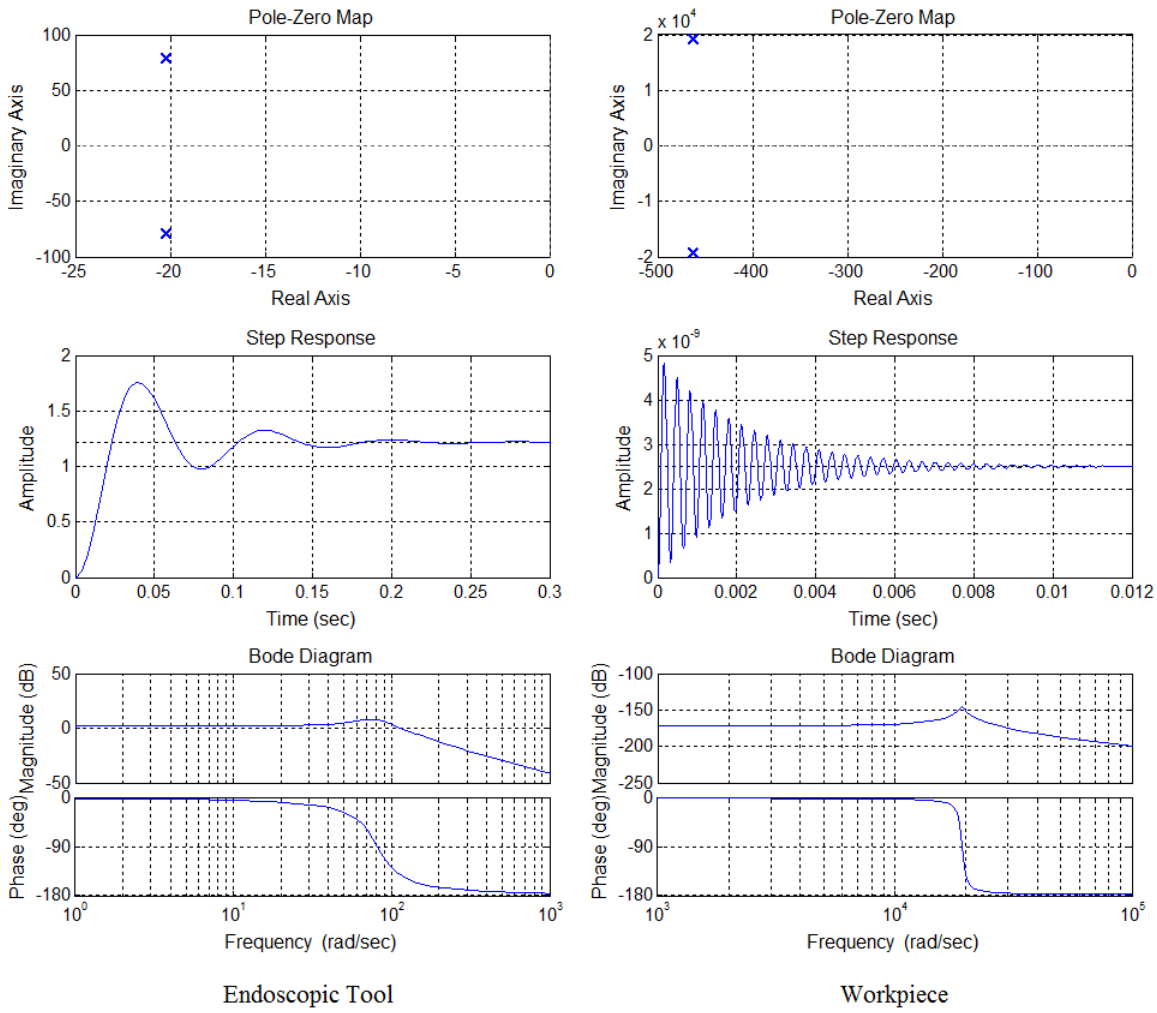

Figure 3.2. Dynamic characteristics of endoscopic tool and workpiece

ter) can be visualized in a chart of the axial depth-of-cut as a function of the spindle speed. This chart is also known as the Stability Lobes Diagram (SLD) or stability chart, as shown in Figure 3.3. The chart reveals the relationship between cutting stiffness and spindle speed. By using this diagram, it is possible to figure out a group of optimized machining parameters that permits maximum chatter-free Material Removal Rate (MRR). In the SLD, there exists a depth-of-cut below which the cut is stable for all spindle speeds. This condition is defined as global stability limit: the maximum cutting stiffness (or depth-of-cut) which gives stable operation for all rotational speeds [26]. Furthermore it can be seen that the lobes get broader and higher as the spindle speed increases. Therefore, by using high speed machining technology, it is possible for the machinist to choose a working point in the peak of such a lobe and hence to increase the MRR. For conventional milling, i.e. at low spindle

speeds, the lobes are too low and too narrow to make use of this benefit. Hence, the introduction of high-speed milling has resulted in a renewed scientific interest in chatter in machining in the 1990s [55].

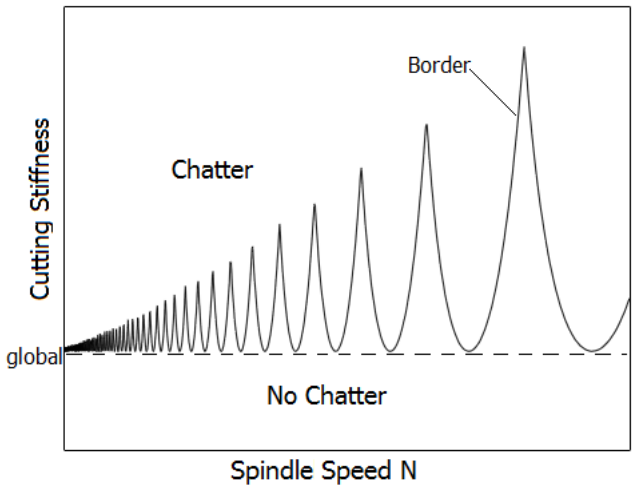

Figure 3.3. Stability lobes diagram (i.e. stability chart)

The SLD is created using regenerative chatter theory, which is usually applied to cutting or milling process that creates chips of various thickness. In orthogonal cutting processes, the cutting force F is proportional to the cutting area, which is a product of the chip width b and chip thickness h. As shown in equation 3.4.1, F is the normal cutting force, k_s is the cutting stiffness in N/mm^2, $x(t)$ is the tool position at time t, and T is the time interval between current cut and previous cut.

$$F = k_s bh = k_s b[x(t-T) - x(t)] \tag{3.4.1}$$

Equation 3.4.3 is called the frequency response function (FRF), derived from the simple dynamic equation 3.4.2 of the cutting process.

$$m\ddot{x} + c\dot{x} + kx = F \tag{3.4.2}$$

$$\frac{x}{F} = \frac{1-r^2}{k[(1-r^2)^2 + (2\zeta r)^2]} + i(\frac{-2\zeta r}{k[(1-r^2)^2 + (2\zeta r)^2]}) = \Re(G) + i\Im(G) = G \tag{3.4.3}$$

In equations 3.4.1, 3.4.2 and 3.4.3, m is the mass of machining system and c is damping coefficient. Tool stiffness is presented by k ($k = F/x$), while r stands for the ratio of chatter

frequency to natural frequency ($r = f/f_n$) of the machining system. Finally, ζ is the ratio of the damping coefficient to the critical damping coefficient ($\zeta = c/c_c$), which is designated by $c_c = 2\sqrt{km}$. Equations 3.4.4 and 3.4.5 describe the chip width b assuming the normal machining force F in equation 3.4.1 is a unit value 1, and the critical value b_{global} below which the cutting process is unconditional stable [56] (free of regenerative chatter). Equation 3.4.6 is the ratio of chatter frequency f and tooth-stroke frequency f_t. According to regenerative chatter theory, chatter will occurs whenever there is a shift of the phase angle ε between current and previous cut, and the vibration amplitude will grow from one revolution to the next when $x(t) > x(t-T)$ [57].

$$b = \frac{1}{k_s(x(t-T) - x(t))} = \frac{-1}{2k_s\Re(G)} \tag{3.4.4}$$

$$b_{global} = \frac{-1}{2k_s\Re(G_{min})} = \frac{2k\zeta(1+\zeta)}{k_s} \tag{3.4.5}$$

$$\frac{f}{f_t} = \frac{r}{r_t} = n + \frac{\varepsilon}{2\pi} = n + \frac{1}{2} + \frac{1}{\pi}tan^{-1}(\frac{-2\zeta r}{1-r^2}) \tag{3.4.6}$$

From equations 3.4.3, 3.4.4 and 3.4.6, the governing equations of SLD can be found, as shown in equation 3.4.7. The parameters are $k = 6$ (N/mm), $k_s = 750$ (N/mm^2) for 6061-T6 Aluminum[57], $\zeta = 0.05$, $n_t = 60$(teeth/rev) and $f_n = 13$ (Hz). n_t designates the number of teeth on the cutting tool. For a grinding stone, it has numerous tiny abrasive particles bonded on it surface. Therefore, in this case the number 60 is not an accurate number, but used only for simulation purpose. After the parameters were applied in the SLD governing equation 3.4.7, the stability lobe diagram could be plotted as Figure 3.4.

$$\begin{cases} b = \dfrac{-1}{2k_s\Re(G)} = \dfrac{k[(1-r^2)^2 + (2\zeta r)^2]}{2k_s(r^2-1)} \\ N = \dfrac{f}{(\frac{n_t}{60}) \cdot [n + \frac{1}{2} + \frac{1}{\pi}tan^{-1}(\frac{-2\zeta r}{1-r^2})]} \\ r = f/f_n \end{cases} \tag{3.4.7}$$

The dash line $global$ in Figure 3.4 is the global critical chip width value below which the grinding process is free of chatter no matter how fast the spindle speed. The solid line segments, which look like lobes, mark the boundary of stable and unstable machining. The area below the boundary is safe (chatter free) for machining, while the upper portion is unstable (suffering from

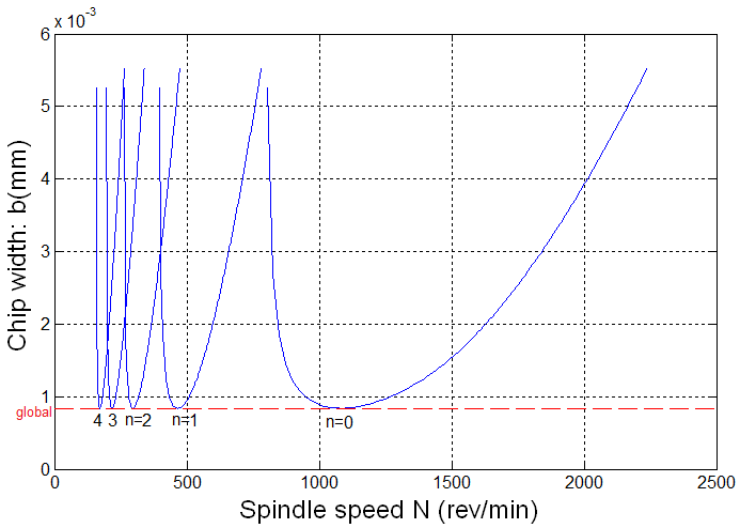

Figure 3.4. Stability lobes diagram of endoscopic grinding model

chatter). If the machining parameter happens to fall on the boundary line, it is considered critical. This diagram suggests that by making use of the safe area in between two lobes, say about 750 rev/min in Figure 3.4 in between lobe (n=0) and lobe (n=1),the value of chip width could be increased by more than 4 times (from 1 μm to 5 μm) without inducing any chatter. It also suggests that by increasing spindle speed, the chip width could be increased and higher material remove rate can be achieved.

3.5 Chatter Detection

In this section a new method is proposed for on-line chatter detection of non-rigid endoscopic tool. According to the proposed scheme, only two sensors were incorporated with the modified endoscope, the LVDT sensor and the force sensor. When the driving cable is locked during grinding process, its displacement could be ignored, therefore the LVDT sensor was not sensitive to any vibration and only the load cell sensor was used for chatter indication.

In grinding process, the force measured by the load cell sensor comprises five components. The internal force is denoted by F_{int} and the static bending force is denoted by F_S, which were introduced in the previous chapter. It is assumed that the fundamental dynamic grinding force is a sinusoidal force $F_d = A_1 sin(2\pi f_1 t + \phi_1)$, and the harmonic vibration force is $F_c = A_2 cin(2\pi f_2 t + \phi_2) + A_3 cin(2\pi f_3 t + \phi_3) + ... A_n cin(2\pi f_n t + \phi_n)$ $(n \in N)$, where function $cin(t)$ is an abstract periodic function describing the vibrating force induced by chatter and

measured on the driving cable. When chatter is observed, the grinding tool head will lose constant contact and bounce against the surface of the workpiece. This action can be modeled as a impulse. The response force F_δ measured by the load cell will be the impulse response force for the dynamic response of the driving cable assembly. The sum of all force components measured by load cell is modeled as equation 3.5.1.

$$\begin{aligned} F_{sum} &= F_{int} + F_s + F_d + F_c + F_\delta \\ &= F_{int} + F_s + F_\delta + A_1 sin(2\pi f_1 t + \phi_1) \\ &\quad + \sum_{n=2}^{N} A_n cin(2\pi f_n t + \phi_n) \end{aligned} \tag{3.5.1}$$

Since the control knob is locked when endoscopic tool was engaged in the grinding process, the internal force F_{int} and the static bending force F_s were constants. The dynamic grinding force F_d and the harmonic vibration force F_c were the $1st$ to nth harmonic force induced by the motor, and they all shared the same base frequency $f_n = f_{motor}$.

The results from the dynamic model section (Fig. 3.5) show that the endoscopic tool is a stable system with high damping ratio. In such a system, the amplitude of the induced harmonic force will decay very quickly. Therefore, only the fundamental force and the 2nd harmonic force will be considered for simplicity. To study the dynamic characteristics, F_{int} and F_s could also be ignored. Assuming the driving cable assembly has a flat frequency response, the periodic impulse force could be modeled as white noise $RND(t)$ in time domain; and since it is a secondary force component, it should have a low amplitude ε. Finally, the force measured by the load cell senor can be described by equation 3.5.2.

$$F_{sum} = A_1 sin(2\pi f_1 t + \phi_1) + A_2 cin(2\pi f_2 t + \phi_2) + \varepsilon RND(t) \tag{3.5.2}$$

Because F_{sum} only contains periodic signals and their linear combination, F_{sum} is a stationary signal. By taking a FFT (Fast Fourier Transform) $FFT\{F_{sum}\}$, the chatter could be detected in frequency domain. Figure 3.5 is plotted from the following parameters; $A_1 = 1.0$, $A_2 = 0.8$, $cin(t) = sawtooth(t, 0.9)$ ($sawtooth()$ function in Matlab), $\varepsilon = 0.3$, $f_1 = f_2 = 50$ Hz, $\phi_1 = 0$ and $\phi_2 = \pi/10$.

According to Figure 3.5, E_{1st} is defined as the value of first peak and E_{2nd} the value of second peak. Equation 3.5.3 is a relative energy indicator of chatter detection where R is the ratio

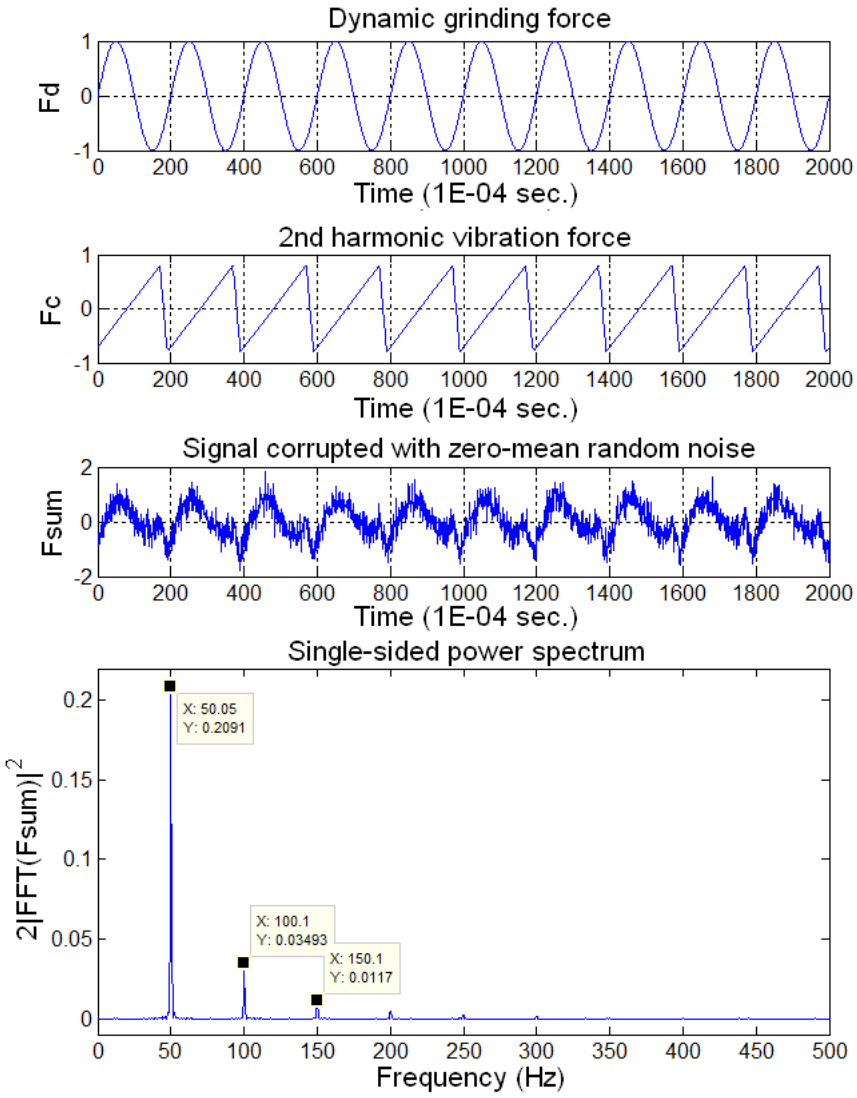

Figure 3.5. Chatter detection model

of first peak value to the second peak value and T is the threshold of observable or unacceptable chatter.

$$R = \frac{E_{1st}}{E_{2nd}} > T \tag{3.5.3}$$

In Figure 3.5, $E_{1st} = 0.2091$ and $E_{2nd} = 0.03493$. The calculated energy ratio $R \approx 5.99$. If the detection threshold $T = 10$, apparently, there are unacceptable chatter in the grinding process described by this figure, because $R < T$ and the amplitude of vibration force F_c has reached 80% of

the amplitude of the dynamic grinding force F_d. The vibration force F_s will seriously degrade the outcome of this grinding process. If the amplitude of vibration force was well suppressed and the phase shift ϕ_2 was in a preferable range, the energy ratio R will become much greater than T and the chatter will drop below observable level. This phenomenon is verified by following experimental results.

Equation 3.5.3 is a simple but effective energy indicator for automatic on-line chatter detection. By taken a FFT on only a few grinding cycles, the energy ratio could be calculated and compared to a user specified chatter threshold T. The computing process can be done in a real-time manner and the detection latency is $t = n/(f_{motor})$. Suppose three cycles of load cell signal is taken for chatter detection, where $n = 3$. When grinding a workpiece at a speed of 5000 rpm, the detection lag is only 36 ms, much faster than a human operator. Since the energy indicator is highly sensitive to chatter, early stage vibration could be found and actions could be taken to prevent it from growing larger. Since R is a relative ratio of machining power, it will be robust no matter how large or how little the absolute machining power, as long as the machining power is within the measurable range. Because the threshold T is dynamically adjustable, this method can be applied to different machining parameter settings when cooperating with an adaptive approach.

3.6 Experiment Setup

3.6.1 Data Acquisition System

The data acquisition system (DAQ) consisted of six major devices: (1) dynamometer, (2) two charge amplifiers, (3) LVDT sensor, (4) load cell and (5) analog-to-digital (A/D) hardware and (6) personal computer (PC & software), which are shown in Figure 3.6 The LVDT sensor and the load cell are the same used in Chapter 2. Four channels of input signal were sampled by the A/D hardware at 10 KHz sampling rate and recorded by a PC for later processing.

3.6.2 Workpiece Installation

A KISTLER 9272 dynamometer was employed to measure the normal force (f_n) and the friction force (f_c) imposed on an aluminum workpiece mounted on it. The aluminum workpiece was rigidly mounted on the dynamometer with its long edge aligned with dynamometer's F_y direction and the face A normal to the F_x direction, as shown in Figure 3.7.

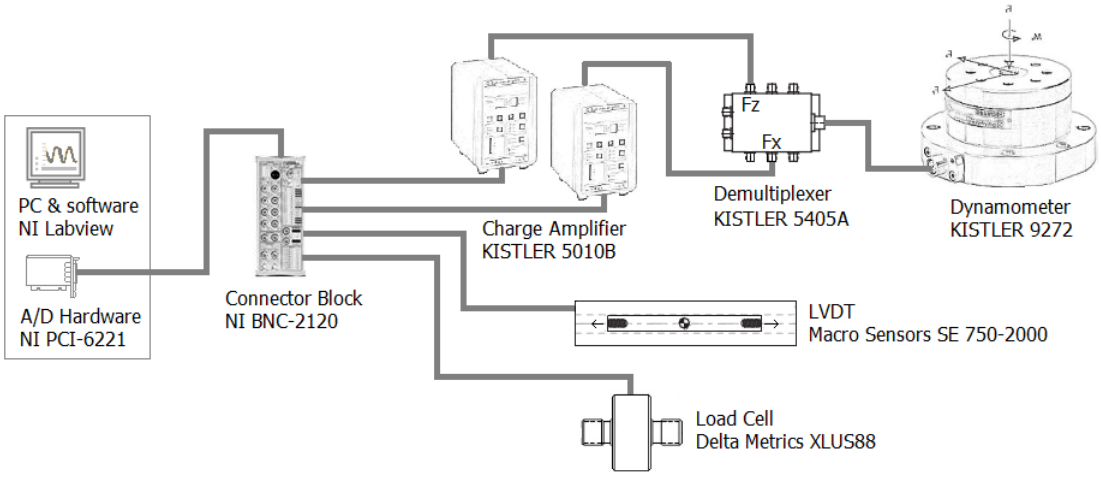

Figure 3.6. Data acquisition system

Figure 3.7. Workpiece mounted on dynamometer

During the machining process, the endoscopic tool was setup to grind on face A (do not duplicate variables), which is normal to F_x direction. The workpiece was mounted across the center point of the dynamometer and the grinding spot was in the center of face A. In this case, the grinding friction force f_c was equal to the force F_z and the grinding thrust force was equal to the normal force F_x measured by dynamometer. If the workpiece was not mounted strictly across the center of the dynamometer, or if the grinding spot is not on the very center of face A, the friction force and the normal force will comprise a torque-moment term $M_y \cdot d_x$ and $M_z \cdot d_y$ respectively, as shown in equation 3.6.1. However, since the moments d_x and d_y were small, neglecting the torque-moment terms did not introduce large error.

Table 3.2. Selected technical data of KISTLER 9272 dynamometer

Measuring range	F_x, F_y	kN	$-5...5$
	F_z	kN	$-5...20$
	M_z	N·m	$-200...200$
Threshold	F_x, F_y	N	< 0.01
	F_z	N	< 0.02
	M_z	mN·m	< 0.2
Sensitivity	F_x, F_y	pC/N	≈ -7.8
	F_z	pC/N	≈ -3.5
	M_z	pC/N·m	≈ -160
Linearity, all ranges		%FSO	$< \pm 1$
Hysteresis, all ranges		%FSO	< 1
Rigidity	c_x, c_y	kN/μm	≈ -0.4
	c_z	kN/μm	≈ -2
	cM_z	kN/μm	≈ -0.7
Natural frequency (mounted on rigid base)	$f_n(x, y)$	kHz	≈ 3.1
	$f_n(z)$	kHz	≈ 6.3
	$f_n(M_z)$	kHz	≈ 4.2

Note 1: Note: Taken from KISTLER's datasheet [58].
Note 2: FSO is Full Scale Output.

$$\begin{cases} f_c = F_z - M_y \cdot d_x \approx F_z \\ f_n = F_x - M_z \cdot d_y \approx F_x \end{cases} \tag{3.6.1}$$

3.6.3 Dynamometer and Charge Amplifier Setup

The four-component dynamometer (KISTLER, Type 9272) is a piezoelectric sensor based equipment, which measures a torque M_z and three orthogonal force components F_x, F_y and F_z. It has a relatively large measuring range with high sensitivity and good linearity and hysteresis [58]. However, the official datasheet does not specify its analog bandwidth, therefore an impulse test [57] was conducted to discover its bandwidth (the bandwidth of measuring system). Table 3.2 shows selected technical specifications of the dynamometer. The output of the dynamometer was connected to a demultiplexer (KISTLER, Type 5405A) to split the F_x and F_z channels to two charge amplifiers, as shown in Figure 3.6.

The charge amplifier (KISTLER, Type 5010B) is a versatile, line-powered, dual mode amplifier for use with high impedance (charge mode) or low impedance (voltage mode) sensors. It works in charge mode with a long time constant setting throughout all following experiments. In charge mode, the unit converts the input charge signal into a voltage proportional to the measurand.

Table 3.3. Selected technical data of KISTLER 5010B charge amplifier

Measuring range	pC	$\pm 10...999000$
Sensor sensitivity	pC/MU	$0.01...9990$
	mV/MU	$0.01...9990$
Input voltage max.	V	50
Input insulation resistance	Ω	10^{14}
Output voltage range	V	± 10
Output impedance	Ω	100
Frequency response: (3dB) standard filter Type 5311	Hz	180000
Accuracy (Long time constant)	%	$\leq \pm 0.50$
Long time constant	sec	$0...100000$
Medium time constant	sec	$1...10000$
Short time constant	sec	$0.01...100$

Note: Taken from KISTLER's datasheet [59].

The long time constant setting permits the user to measure short duration static (quasi-static) events [59]. With a standard filter installed, the analog bandwidth, the 3dB frequency response in Table 3.3 of the charge amplifier is set to 180 KHz, which is much higher than the 10 KHz sampling frequency of the DAQ system.

An impulse test was conducted to test the frequency response and bandwidth of the DAQ system. There are four data sampling channels in this DAQ system: an LVDT channel, a Load cell channel and two force measurement channels from the dynamometer through charge amplifiers. In a single channel, the devices with the most limited bandwidth boundaries will define the overall bandwidth of that channel. For example, the LVDT channel comprises two components – the LVDT sensor and the A/D hardware. The 3dB frequency response of the LVDT sensor is 250 Hz according to its datasheet [60], and the A/D hardware's sampling rate is set to 10 KHz for all channels. In this case, the LVDT channel will have a bandwidth of 250 Hz.

A force measurement channel consists of a dynamometer, a demultiplexer, a charge amplifier and A/D hardware. To discover the overall frequency response and bandwidth of the entire channel is more valuable and convenient than finding out the bandwidth of each component. An impulse test was conducted for this purpose. During the test, the dynamometer was fixed on an rigid base, then a hammer was struck on the X and Z direction of the dynamometer. The frequency response was acquired by recording the voltage output of the A/D hardware in time-domain. The bandwidth of the overall channel was found by transforming the time-domain response signal to frequency domain.

3.7 Experiment Result

3.7.1 DAQ System Frequency Response

Figure 3.8 shows an impulse response test result in F_x force measurement channel. The hammer was struck in the X direction of the dynamoeter. Although great effort was taken to make this stroke as short as possible, it still can not be an ideal impulse. Furthermore, any amplifier and A/D converter will have zero-point error, which will render the DC component of test result larger than it should be. Bearing this in mind, the test result will not be completely accurate, but still could portray a rough picture of the force channel dynamic response. The single-side power spectrum of Vx shows that the dynamometer has larger gain in low range (<1 KHz), middle range (1.5 KHz-3.0 KHz) and high range (>4.5 KHz). Figure 3.9 was generated using the same method in the Z direction. The difference is that in Z direction the middle range shifted to 1.5 KHz-2.8 KHz high range shifted to 3.5 KHz-4.5 KHz. Finally, it should be noted that there is a strong attenuation point near 1 KHz and 1.1 KHz on X and Z frequency plot for an unknown reason. Fortunately, in most of following experiments, only the low frequency range (<1 KHz) will be used.

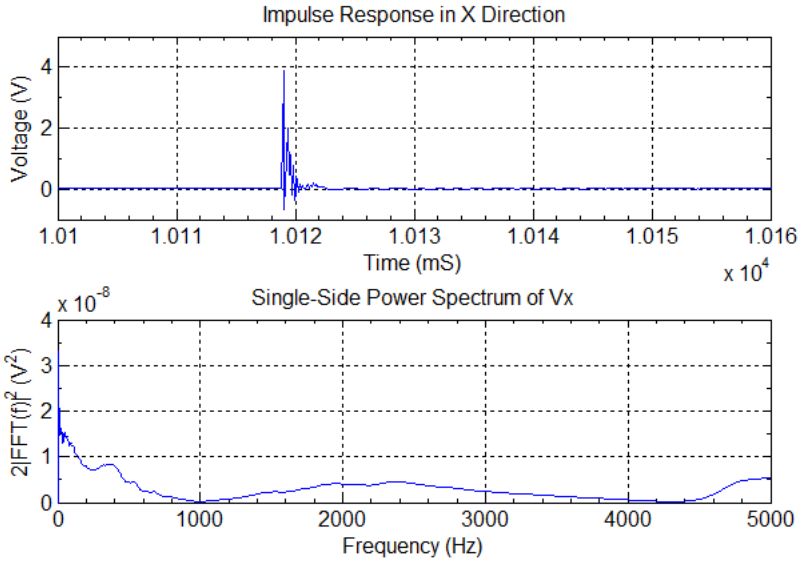

Figure 3.8. Impulse test of force measurement channel (F_x)

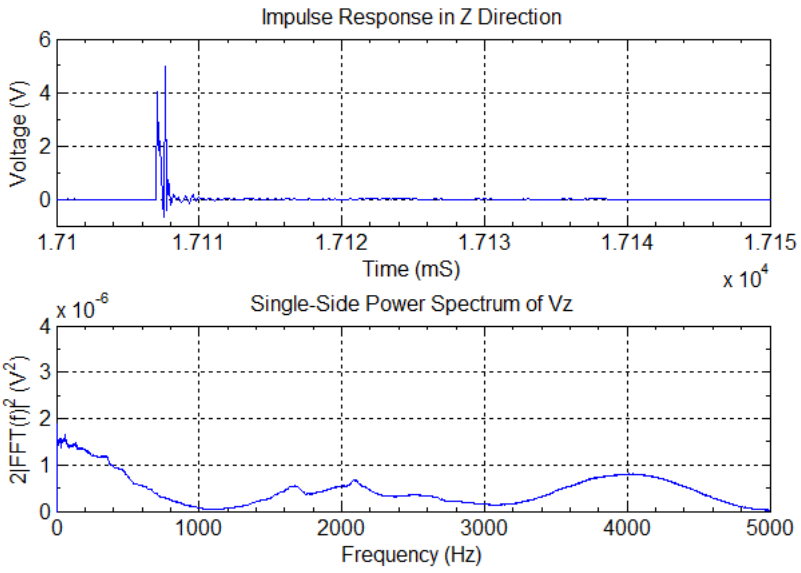

Figure 3.9. Impulse test of force measurement channel (F_z)

3.7.2 Characterization of Tool Head Vibration

Figure 3.10 shows three pictures of grinding tool head rotating at 5K, 10K and 20K rpm respectively with same camera setting. The tool head was constrained in the direction perpendicular to the paper, but was allowed to move freely in the direction parallel to the paper. When the tool head rotation speed increases from 83.3 Hz (5K rpm) to 333.3 Hz (20K rpm), the tool head vibration amplitude decreased from 13.5 degree to 2.3 degree, by about 83 percent. This test shows that when the frequency of machining force goes far away from the natural frequency of the endoscopic tool, which is about 13 Hz found in previous section, the vibration will decrease and the tool head will be more stable.

The results of this test also revealed that endoscopic machining will benefit from high tool head speed, which could stabilize the machining process and enable increased MRR. The only concern in the experimental configuration is that the power was transmitted from an external Dremel motor to the grinding stone by a flexible steel shaft. When the bending section was bent to 90 degree or more and the shaft is rotating at such a high speed, the metal fatigue will break the shaft in a short time. Two possible alternative solutions are substituting the power transmission shaft with a pneumatic driving system or using a low profile motor mounted on the tip of endoscope bending section instead of external motor. A pneumatic driving system like the one used on dental drill could boost the rotation speed up to 300K to 400K rpm [61].

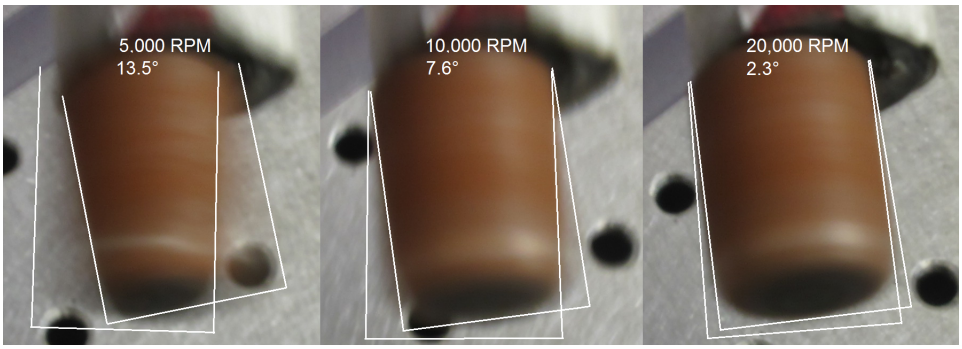

Figure 3.10. Amplitude of tool head vibration

5000 rpm:13.5^o 10,000 rpm:7.6^o 20,000 rpm:2.3^o

(Canon PowerShot G11, f/7.1, 1/2 sec., ISO-80, focal: 6 mm, aperture: 2.96875)

3.7.3 Detection and Analysis of On-line Grinding Chatter

Figure 3.11 shows a piece of raw data of a 30 s grinding process on a 6061 aluminum workpiece measured by the load cell installed on the endoscopic tool. A rough picture of the machining procedure is described by this piece of data. The X axis scales the time and the Y axis is voltage signal measured by load cell sensor. The ramp between 5 s to 7 s in Figure 3.11 indicates that the endoscopic tool is bending to and approaching the workpiece. Since the tensile force on the driving cable is gradually increasing while pulling the grinding tool to the workpiece surface, the force (voltage) measured by the load cell sensor is also increasing in a ramp. From 7 s to 37 s, the plateau indicates the grinding process lasts for approximately 30 s. As the voltage is proportional to the normal machining force, the normal machining force is nearly constant from 20 s to 35 s. The sudden drop at 37 s means the grinding tool head was removed from the surface of workpiece promptly.

Figure 3.12 shows a small region of data taken from the plateau in Figure 3.11. The amplitude of this region is about 800 μV peak-to-peak. In Figure 3.12, the DC base of this signal, which is about 11mV read from Figure 3.11, has been removed. The time duration of this region is about 25 ms, from 19.11 s to 19.36 s.

Since the 25 ms time duration was short enough and this short piece of signal $v(t)$ could be assumed to be stationary, the machining parameters were not likely to suddenly change during this time duration. Therefore, a Fourier transform could be applied to it. The result of $FFT\{v(t)\}$ (Fast Fourier Transform) reveals the frequency domain composition of signal $v(t)$. In the single-side power spectrum of the load cell data in Figure 3.12, the X axis is frequency in Hertz, and the

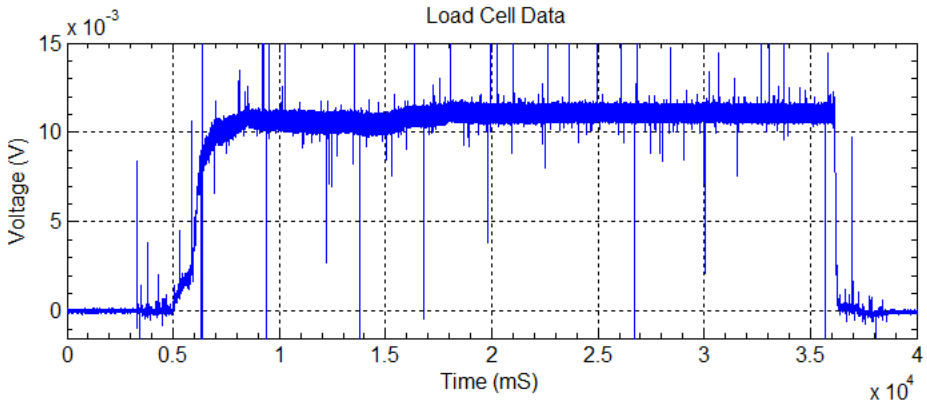

Figure 3.11. Load cell measurement data from grinding experiment

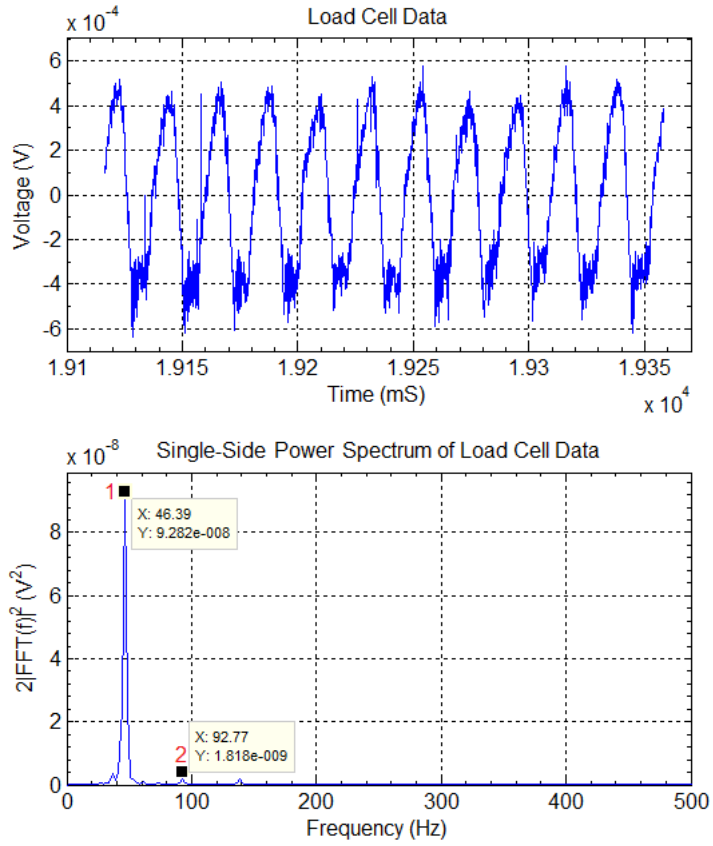

Figure 3.12. Load cell sensor data of grinding sample #8 (DC base removed)

Y axis is the power $Y = 2 \times ABS(FFT\{v(t)\}^2)$ of the unit V^2. The first peak in Figure 3.12 is where the most of grinding energy is concentrated and the fundamental frequency f_1 is 46.39 Hz,

which is the rotational speed of grinding tool. The second peak is caused by harmonic vibration and its frequency is the 2nd harmonic frequency, which is 92.77 Hz, twice as much as the fundamental frequency.

R is an energy ratio of fundamental grinding power to the second harmonic vibration power. As R increases, the amount of energy contributed to grinding increases and the amount of energy wasted on chatter decreases. Setting $T_{Low} = 10$, $T_{High} = 30$ as global chatter power thresholds for unacceptable and acceptable grinding process, respectively, for experiments, equation 3.7.1 shows that the energy ratio of grinding process in Figure 3.12 is acceptable because R is greater than T_{High}.

$$R = \frac{E_{1st}}{E_{2nd}} = \frac{9.282 \times 10^{-8}}{1.818 \times 10^{-9}} \approx 51.1 > T_{High} \quad (T_{High} = 30) \tag{3.7.1}$$

In contrast, Figure 3.13 shows a grinding process suffering from unacceptable chatter, where the energy ratio R calculated in equation 3.7.2 is less than T_{Low}.

$$R = \frac{E_{1st}}{E_{2nd}} = \frac{3.27 \times 10^{-9}}{6.006 \times 10^{-10}} \approx 5.4 < T_{Low} \quad (T_{Low} = 10) \tag{3.7.2}$$

Frictional grinding force data from reference channel (Dyanmometer Fz channel) is presented in Figure 3.14 to verify the effectiveness of R. The frictional grinding force corresponding to sample #8 was wavy but continuous and no obvious chatter could be identified. In contrast, frictional grinding force corresponding to sample #9 was impulse like and discontinuous, which means the grinding process had already become unstable and the tool head was bouncing against the workpiece surface. Obvious chatter was identified.

Figure 3.15 shows a close examination of aluminum sample number 8 and 9 after 30 s of grinding. The ground texture of sample number 8 looks like several grooves cut in the same direction, while that of sample number 9 looks like numerous random strokes imprinted on workpiece surface and each stroke corresponds to an impulse envelop in Figure 3.14. More experiments have been done to verify the effectiveness and performance of the energy ratio indicator. Since their results are quite similar to those of sample number 8 and 9, their figures are not presented here. But their result will be used in the next chapter in the calculation of MRR.

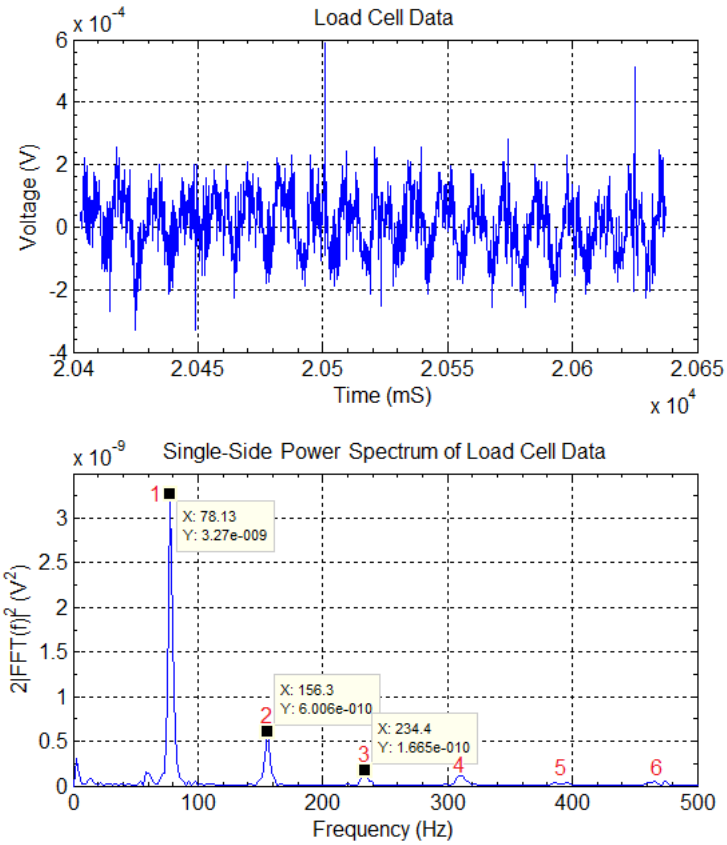

Figure 3.13. Load cell data of grinding sample #9

3.8 Conclusions

In this chapter the study of the dynamic characteristics of endoscopic tool was presented. The natural frequency of endoscopic tool was found to be 13 Hz from the dynamic model. Since some parameters used in the dynamic model had to be guessed, the 13 Hz value is only an approximate estimate. But, a confident conclusion can be made that the natural frequency of endoscopic tool is within 10 Hz to 100 Hz range. The tool head vibration test results proved that when the frequency of machining force deviated from the natural frequency (from 83.3 Hz to 333.3 Hz), the chatter amplitude decreased (from 13.5^o to 2.3^o).

Regenerative chatter theory was applied to predict the chatter in grinding process. The calculated result showed that the regenerative chatter was not a dominant factor in grinding process, because the cutting width b was almost always below the global threshold b_{global}. Therefore, the major vibration was generated by the grinding tool itself.

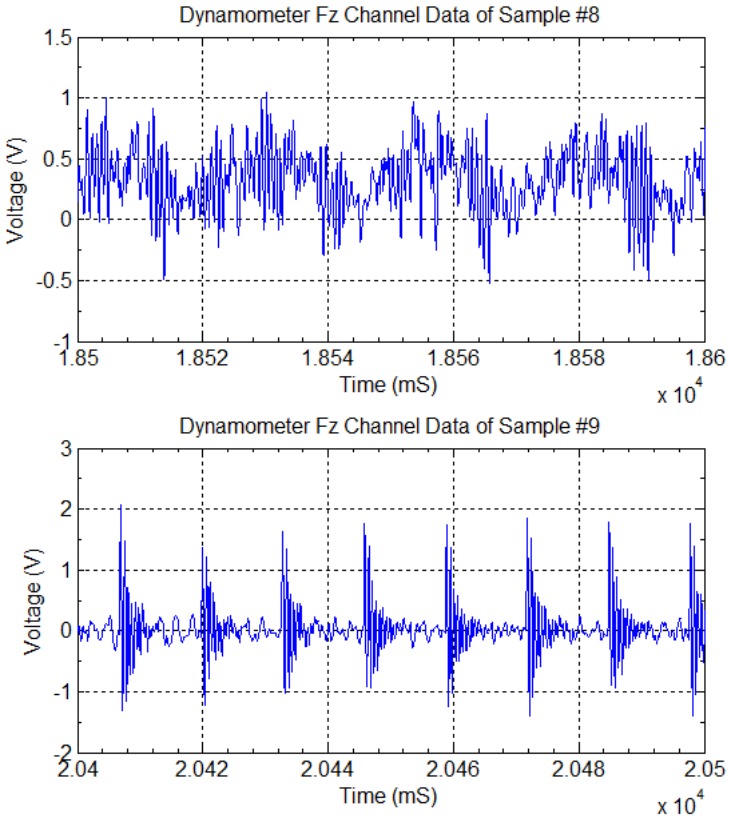

Figure 3.14. Dynamometer Fz frictional grinding force data

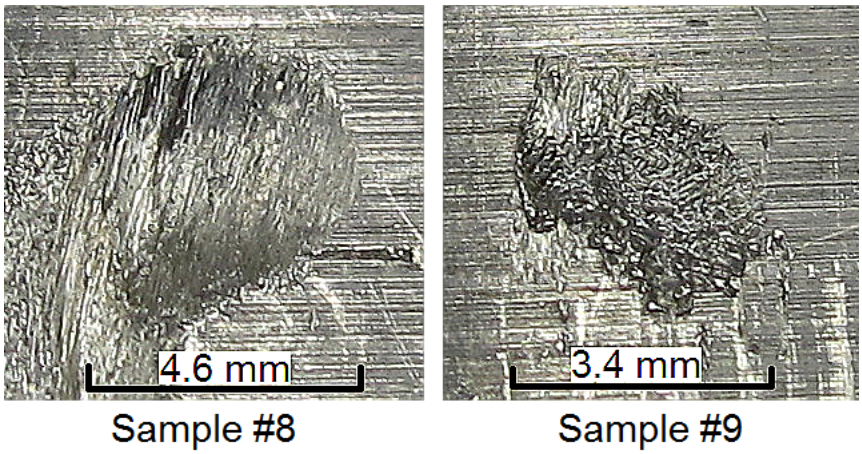

Figure 3.15. Workpiece surface after grinding (sample #8 and #9)

An on-line chatter detecting method called relative energy ratio indicator was proposed to automatically discover the early stage chatter in grinding process. The energy indicator was highly

sensitive to chatter, robust to different grinding parameter settings, and of low computational cost. The effectiveness and performance of this method was verified by experiment results. From the most stable grinding process to the worst case, the relative energy ratio varied from 51.1 to 5.4, which meant high resolution of the proposed method.

Increasing the grinding tool speed benefited the stabilization of the endoscopic tool as well as the MRR. In the future, a pneumatic driving system could be employed to boost the machining speed up to 300K to 400K rpm. As another alternative, a bending section tip mounted motor could be substituted for the current external Dremel motor to resolve the fatigue problem of power transmission shaft. Other methods such as active damping may also be helpful.

Chapter 4

Quantification of Material Removal With Non-Rigid Machining System

4.1 Introduction

There are many quantitative criteria of machining, such as geometric accuracy, surface roughness, material removal rate (MRR), energy efficiency etc. In an application like jet engine crack smoothing, it is necessary to know the mass of material removed on each turbine blade. In conventional machining, MRR is defined as the volume of material removed in one unit of time [62] and a common unit is mm^3/second. In a Computer Numerical Control (CNC) machining center, the position of tool head is precisely controlled at μm scale. For a simple task, where the workpiece is of a simple geometric shape and the tool head started from (x1, y1, z1) and machined to (x2, y2, z2) by following a route R, the volume of material removal and the MRR could be easily calculated by integrating volume by route and then divided by time. Sometimes, it is possible, but difficult, to calculate the material removal by using the geometric approach when the workpiece is of a non-simple shape – for example, a turbine blade with curved aerodynamic surface bearing a crack of arbitrary shape. One could find out the material removal by gathering and weighing every piece of debris and chip generated in the crack smoothing process, but a dedicate chip gathering mechanism and a high accuracy scale would be required. An alternative method to calculate the material removal is to divide the total machining energy by the specific energy of the material under machining. This empirical and calibrated energy approach is very common in traditional machining, and many data and charts are available for certain kinds of machining and material types [43]. However, in endoscopic machining, the specific energy approach has not been proposed

and evaluated. In this chapter, an energy based MRR prediction model of endoscopic machining (grinding) and its experimental evaluation is presented.

4.2 Literature Review

Zhang and Pan [63] proposed a practical MRR control method based on experimental identified dynamic model and force and power feedback control, which reduces the vibration and dramatically increases the productivity of robotic machining process. The dynamic model of a six-degree-of-freedom robotic manipulator in milling process is complex enough to be built analytically, so they identified the model via experiments. Results shows that Zhang's approach is quite effective and practical.

Song et al. [64] found that due to a variety of factors, such as workpiece shape, contact force, robot velocity and belt wear, precise control of material removal for free-formed surfaces (e.g., surface of turbine blades and artificial metal joints) using a robotic belt grinding system can be very challenging. The author proposed an adaptive modeling method to off-line plan the control parameters for high-quality material removal control of robot grinding system. The removal errors of the grinding points in stable grinding process were less than 0.05 mm. Challenges of precisely controlling the MRR in semi-rigid machining was recognized and addressed. However, most of existing research efforts are based on robotic applications and their models and experiment approaches are not applicable for endoscopic non-rigid tools. Therefore, dedicate MRR prediction model of endoscopic tool and effective experiment methods are required.

4.3 Energy Model for Prediction of Material Removal

An energy model is proposed to predict the material removal of endoscopic grinding process. This model needs three inputs and generates one output. The three inputs are driving cable tensile force F_{cell} measured by the load cell, driving cable displacement δ measured by the LVDT sensor and grinding time duration T. The output is predicted mass of material removal M in milligrams. The frictional grinding force F_z and normal grinding force F_x measured by the dynamometer are used only for deriving the model.

In terms of energy, a machining process is considered efficient if material is removed quickly at the cost of low energy consumption. The specific energy is commonly used as an inverse measurement of machining efficiency[62].

In machining, specific energy is defined as the ratio of machining power to MRR:

$$Specific\ Energy = \frac{Machining\ Power}{Material\ Removal\ Rate} \tag{4.3.1}$$

In equation 4.3.2 e_s is specific energy, F_t is the tangential force in Newton, v_s is the wheel speed in meter per second and their product P is power in watt. b_w is the width of grinding contact in meter (or commonly millimeter), a_e is the depth of cut in meter (or micron), v_w is the work speed or feed speed in meter per second, and their product is MRR commonly in cubic millimeter per second. Since both power and MRR can be integrated by time, the specific energy expressed in equation 4.3.2 could also be described in terms of energy E and material removal volume V_w as shown in equation 4.3.3, and the SI unit for e_s is joules per cubic millimeter.

$$e_s = \frac{P}{MRR} = \frac{F_t \cdot v_s}{b_w \cdot a_e \cdot v_w} \tag{4.3.2}$$

$$e_s = \frac{E}{V_w} = \frac{\int P(t)dt}{\int MMR(t)dt} \tag{4.3.3}$$

As the specific energy increases, the efficiency of the machining process increases. For traditional grinding, the specific energy can vary from 10 J/mm^3 to 100 J/mm^3 for high feed rate grinding to finish grinding or for soft to very hard surfaces [62].

Equations 4.3.2 and 4.3.3 use geometric criterion (i.e. cubic millimeter) for calculation of specific energy. In tasks like crack smoothing, the geometric approach may not be suitable, because the crack may have hard-to-measure, arbitrary geometric shape. It is more convenient to use mass criterion, because it is easy to decide the amount of material removal by weighing the workpiece before and after grinding. Since mass equals volume times material density, specific energy can be related to mass as well as volume of material removal. In endoscopic machining, the input power is the electric power $P(t) = V(t) \cdot I(t)$ and the total input energy E_{in} is the integral of power $P(t)$ by machining time T. Considering the efficiency of motor and power transmission overhead (energy loss on transmission shaft due to bending and friction), the energy spent on grinding is $E_{in} \times \eta_{tool}$, where η_{tool} is the energy efficiency of endoscopic tool.

$$\eta_{tool} = \frac{E_{grind}}{E_{in}} \tag{4.3.4}$$

The energy flow of endoscopic grinding can be illustrated by equation 4.3.5. E_{grind} is the total energy spent on grinding activity, namely useful energy on material removal (chip formation + ploughing + rubbing)[65], and wasted energy on tool chatter and power transmission overhead. E_{in} is the total input energy described by voltage and current input of the grinding motor and η is the energy efficiency coefficient. Hereby the specific energy can be defined as the energy consumption on unit mass of material removal in joules per milligram (J/mg). In such a case E_{in}/M could be defined as gross specific energy and $E_{removal}/M$ is the specific energy of endoscopic grinding. It is thought that if the specific energy of endoscopic grinding is known, the mass of material removal can be estimated with reasonable accuracy.

$$\begin{aligned} E_{grind} &= E_{in} \times \eta_{tool} \\ &= \int_0^T V(t)I(t)dt \times \eta_{tool} \\ &= \int_0^T P_{removal}(t)dt + \int_0^T [P_{chatter}(t) + P_{overhead}(t)]dt \end{aligned} \tag{4.3.5}$$

Equation 4.3.6 defines the force ratio between tangential grinding force (F_t) and normal force (F_n). F_Z and F_X are forces measured by Z-channel and X-channel of the dynamometer. In equation 4.3.7 the tangential force is mapped to δ_{LVDT} and $F_{Loadcell}$, the only two inputs of the MRR prediction model. Assuming F_n is normal to the grinding tool, function $G()$ can be substitute by equation 2.5.13.

$$\mu = \frac{F_t}{F_n} = \frac{F_Z}{F_X} \tag{4.3.6}$$

Then,

$$F_t = \mu F_n = \mu G(\delta_{LVDT}, F_{Loadcell}) \tag{4.3.7}$$

In equation 4.3.8, where $F_t(t)$ is a constant, f_{grind} is a constant rotating speed of grinding tool in Hertz, and D is the tool head diameter, the grinding energy E_{grind} is linear in time.

$$E_{grind} = \int_0^T P_{grind}(t)dt = \int_0^T F_t(t) \cdot v_s(t)dt = F_t \cdot f_{grind} \cdot T \cdot \pi D \tag{4.3.8}$$

Combining equations 4.3.7 and 4.3.8, the grinding energy can be calculated by equation 4.3.9. A part of grinding energy E_{grind} is spent on material removal as energy index E_s, and other

part of grinding energy is wasted due to chatter, as shown in equation 4.3.10. Function $R()$ is the percentage of chatter energy in grinding energy and can be decided by the power spectrum of the grinding energy, which is related to the frequency composition of $F_{Loadcell}$.

$$E_{grind} = \mu(\delta_{LVDT}, F_{Loadcell}) \cdot G(\delta_{LVDT}, F_{Loadcell}) \cdot f_{grind} \cdot T \cdot \pi D \tag{4.3.9}$$

$$E_{grind} = E_s + E_{chatter} + E_{overhead} = E_s + (E_{grind} - E_{overhead}) \cdot R(P_{Loadcell}) + E_{overhead} \tag{4.3.10}$$

Equation 4.3.11 illustrates that the energy index E_s can be mapped to material removal through a coefficient κ and can be calculated in equation 4.3.11, which comprises three functions $\mu()$, $G()$ and $R()$.

$$\begin{aligned} M_{removal} &= \kappa(E_s) = \kappa(E_{grind} - E_{overhead} - E_{chatter}) \\ &= \kappa T f_{grind} \Big\{ (\mu(\delta_{LVDT}, F_{Loadcell}) G(\delta_{LVDT}, F_{Loadcell}) \cdot \pi D - \int_{-\theta}^{+\theta} P_B(\theta) d\theta - E_f) \\ &\quad \cdot R(P_{Loadcell}) \Big\} \end{aligned} \tag{4.3.11}$$

$\mu = \mu(delta_{LVDT}, F_{Loadcell})$ is the ratio of tangential grinding force to normal force and is dependent on grinding parameters such as grinding angle, workpiece material and surface condition, tool grain size, tool wear etc. Assuming the change of grinding parameters are small enough to be neglected for a batch of grinding tasks, the force ration μ will remain the same, and the tangential grinding force is linearly proportional to the normal force F_n. F_n can be calculated by function $G(\delta_{LVDT}, F_{Loadcell})$, and the tangential grinding force F_t and E_{grind} can be decided. The energy overhead is mostly wasted on bending the power transmission cable back and forth in every turn ($2\int_0^{\theta} P_B(\theta)d\theta$) and contact friction between the cable and the endoscope tool channel (E_f). The bending angle θ can be estimated using equation 2.4.1 and 2.5.9, while $P_B(\theta) = \sum_{i=1}^{n} \alpha_i (\theta - \beta_i)^i$ and the bending power coefficient α_i and β_i can be calibrated through experiments.

An important part of the model is the determination of percentage of energy wasted due to the chatter. Both analytical and empirical methods are employed to relate chatter waste energy to the power spectrum of $F_{Loadcell}$.

Figure 4.1 contains the $F_{Loadcell}$ power spectrum of grinding on sample #8 and #9. Most of the grinding energy is concentrated at the first peak in grinding sample #8, which corresponds to

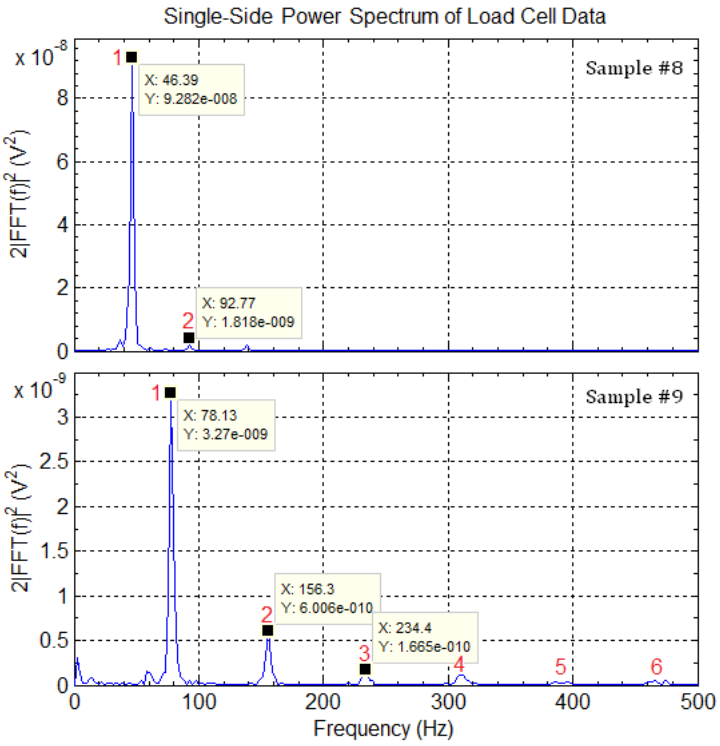

Figure 4.1. Power spectrum of $F_{Loadcell}$

the fundamental frequency of rotary grinding tool. The second and higher order harmonic peaks are observable in grinding sample #9, because of the chatter. Equation 4.3.12 separates chatter waste energy from grinding energy using load cell power spectrum. P_1 is the power of the first harmonic peak. The ith peak has a central frequency located at f_i and the breadth of that peak is from f_i^- to f_i^+ in frequency domain. For sample #8, 99% of its first peak power is in the range of 35 to 60 Hz.

$$E_{chatter} = E_{grind} \cdot R(P_{Loadcell}) = E_{grind} \cdot \left(1 - \frac{\int_{f_1^-}^{f_1^+} \lambda_1 P_1(f)df}{\sum_{i=1}^{N} \int_{f_i^-}^{f_i^+} \lambda_i P_i(f)df}\right) \tag{4.3.12}$$

Since the tensile force measured by the load cell is indirectly related to the grinding energy and the driving cable is a nonlinear component, the $P_{Loadcell}$ should not be directly used in the calculation of chatter energy. Therefore, a set of empirical power compensating coefficients (λ_1 to λ_N) are applied on P_is ($i \in [1..N]$).

In the next section, experiments are conducted to acquire empirical data to specify the force ratio function $\mu()$, power compensating coefficients λ_1 to λ_N and the bending power coefficient α_i and β_i.

4.4 Evaluation of MRR Model Prediction through Endoscopic Grinding Experiment

In the experiments an aluminum workpiece was weighed before and after the endoscopic grinding operation. This measurement of material removed was compared to the prediction of material removed from the model, which used the driving cable force and position measurement during operation as input. The experimental setup was the same as described in chapter 3. One group of endoscopic grinding experiments was conducted to find the parameters in the semi-empirical material removal prediction model. Another two groups of endoscopic grinding experiments was performed to validate the repeatability of the MRR prediction model.

Endoscopic grinding experiment setup is shown in Figure 4.2. The dynamometer is fixed on an optic table and the workpiece is fixed on top of the dynamometer. The endoscope bending section can bend freely in horizontal workspace XOY but is restricted to move vertically. The base point O of the bending section is fixed in between two metal brackets. The workpieces are cut from a 6061-T6511 aluminum bar and each piece is 8 mm$\times 38$ mm$\times 95$ mm in size and 74 g to 76 g in mass approximately. The initial bending angle θ was about 90 degrees and grinding angle φ was set to zero, which means the grind stone was in full contact with the surface of the workpiece. For each grinding test, the motor was set to 5000 rpm (83.3 Hz).

For the procedure, the horizontal control knob was turned to bend the bending section and create the force between the grinding tool and workpiece. The turning force was quickly increased to a preset level and the control knob was locked. At this moment, the grinding stone started to remove material from the workpiece. After 30 s of grinding, the control knob was unlocked and turned counter clockwise to lift the grinding stone off the surface rapidly. Before and after grinding, each workpiece was weighed on a Mettler Toledo XP504 precision scale with 0.1 mg resolution (readability). The decreased value of weight of the ith workpiece was recorded as M_i.

Nine workpieces were ground in the first experiment and the results were taken to calibrate the parameters in the material removal prediction model, as shown in Table 4.1.

Coefficients α_2, α_1 and β_2, β_1 are all zero and, therefore, not listed in the parameter table. In this model, energy index E_s is a dimensionless number, which is indicator to the specific energy.

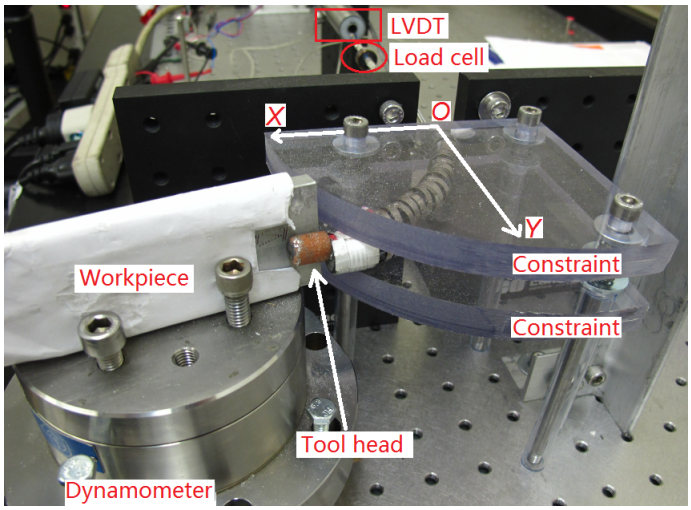

Figure 4.2. Endoscopic grinding setup

Table 4.1. Material removal prediction model parameters

Bending angle (degree)	θ	$(0.6483\delta_{LVDT}^2 + 12.08\delta_{LVDT}2 - 0.0597)/0.5766 + \int F_{Loadcell}(t)dt/1000$
Force ratio	μ	$1.2 \times cos(\lvert\theta - 1.815\rvert)$
Chatter coefficients	λ_1	1
	λ_2	0.9
	λ_3	20
Overhead coefficients	α_3	0.08
	β_3	90
Energy coefficient	κ	$1.3E-03$

Together with M_i, the relationship between $E_s(i)$ and predicted material removal $M_p(i)$ was built to be equation 4.4.1.

$$M_p(i) = \kappa E_s(i) = (1.3 \times 10^{-3}) \cdot E_s(i) \tag{4.4.1}$$

In experiments two and three, $F_{Loadcell}$ and δ_{LVDT} data of each workpiece were recorded and were input into the material removal model to calculate the corresponding $E_s(i)$ and then $M_p(i)$. The weighed results and predicted results will be compared and presented in the result section.

4.5 Comparison Between Measured and Calculated Results

Figure 4.3 shows the measured and calculated results of two experiments in format (E_s,M_i). The solid line is drawn using equation 4.4.1. Therefore, each point on the solid line is (E_s, M_p), and the deviation between M_p and M_i is prediction error. The relative prediction error is defined in equation 4.5.1.

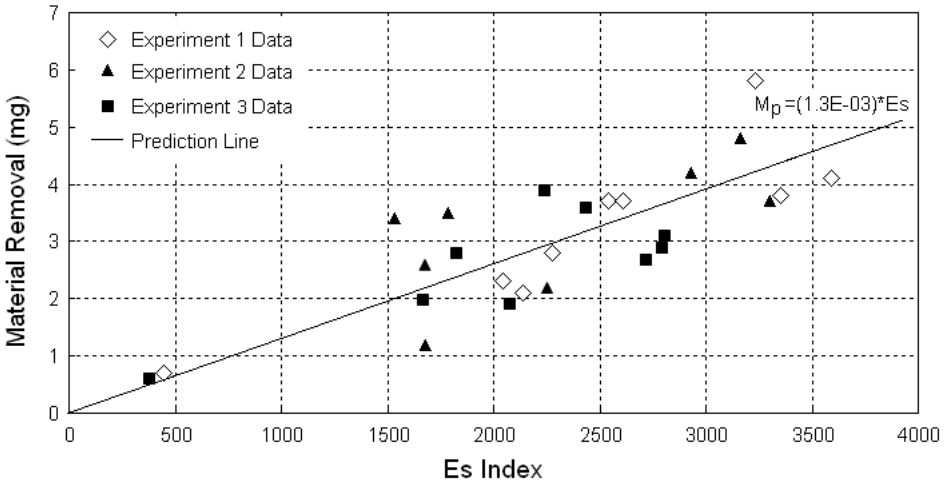

Figure 4.3. Material removal prediction

$$M_{Error} = |M_p - M_i|/M_i \tag{4.5.1}$$

Figure 4.4 shows the relative prediction error. Eight workpieces were ground and weighted during this experiment. The maximum error reaches 41% while the minimum error is 9.2%. The average error is 22%. Note that one result (1.2, 1677) is excluded because it had unacceptable error of 81%. Because its absolute material removal is almost three times lower than that of the average level (3.2 mg), this point is vulnerable to artificial induced errors.

Figure 4.5 shows the energy composition in E_{grind} in comparison with θ. As θ increased, more energy was wasted on bending the power transmission shaft, and so $E_{overhead}$ increased as well. For each grinding task, the initial grinding angle was zero. But the grinding angle was increased to increase the force to keep the grinding tool stable or to increase MRR, which means the grinding stone was not always in full contact with the surface under machining. θ was also influence μ and it was found that 105 degrees and 116 degrees were preferable bending angles, which led to greater MRR.

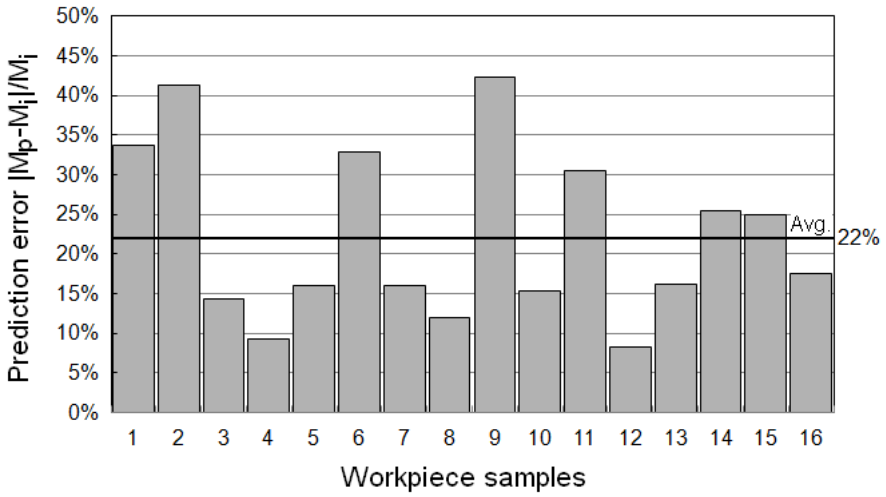

Figure 4.4. Material removal prediction relative error

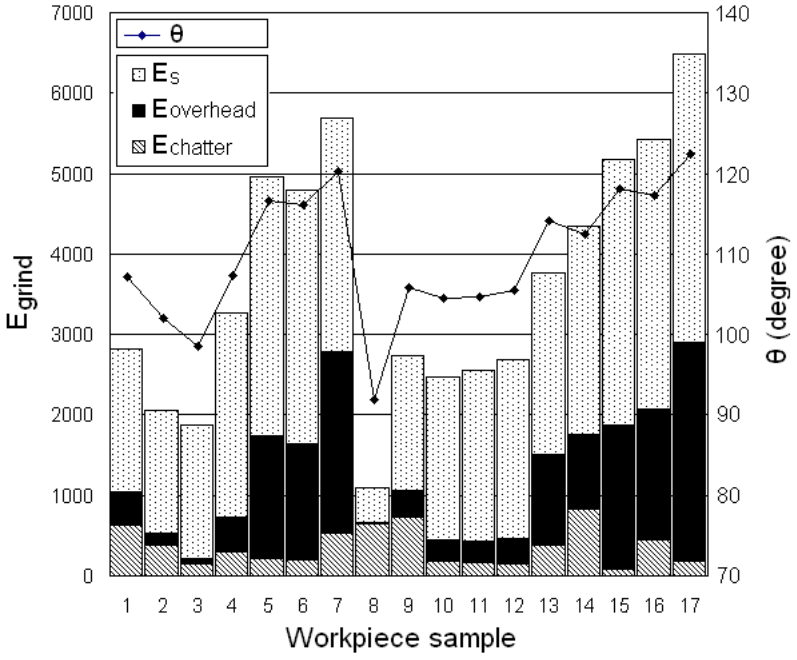

Figure 4.5. E_{grind} composition in comparison with θ

In Figure 4.5, when E_{grind} is low, which means F_n is also low, $E_{chatter}$ is going to occupy a large part of E_{grind}, such as in workpiece sample 8.

4.6 Conclusions

A semi-empirical material removal model was formulated and evaluated. $F_{Loadcell}$ and δ_{LVDT} were the two inputs and the output was M_p. An analytical method was applied to build up the model and grinding experiments were done to calibrate model parameters. Another set of experiments was conducted to validate the repeatability of the model. The comparison of the experimental and theoretical results showed that the average predicting error ratio is 22%.

Endoscopic grinding was proved a valid way to remove material from a workpiece. In current experimental setup, a simple calculation revealed that the specific energy is much higher than in conventional grinding, caused by the bending and friction of the power transmission shaft with the bending section during grinding, which inevitably meant significant amount of energy overhead. The shaft suffered from fatigue during grinding process and when motor speed increased to more than 10,000 rpm, the shaft would not last a long time before failure.

Grinding energy E_{grind} was calculated using its physical definition (force acting through a distance). The force ratio μ was modeled as a function of the bending angle θ and calibrated through experiments.

Chatter energy $E_{chatter}$ was modeled as a fraction of E_{grind}, which was indicated by the high order harmonic peaks on the grinding energy power spectrum. Chatter was more obvious and occupied more energy than in traditional grinding practices, due to the low rigidity of the endoscopic grinding tool. Chatter will occur and grow when the normal force is insufficient to suppress the tool vibration. In the worst case, chatter energy was more than 50% of the total input energy, causing very low MRR. This situation was caused by the very low normal force, which was intentionally set for experiment purpose and is unlikely to be used in normal grinding tasks. Therefore, chatter is an important but not a primary problem in endoscopic grinding.

The energy overhead $E_{overhead}$ is due to the flexible power transmission shaft, which runs through the entire work length of the endoscope from the tool insertion port on the handler to the tip of bending section. During experimental machining processes, the power transmission shaft was rotating and the friction force between the shaft and the plastic tube of tool channel was significant in the bending section, where high contacting (bending) force caused high frictional force between the shaft and the plastic tube. Meanwhile, the energy spent on yielding the rotating shaft to the bending angle from cycle to cycle was also significant and would cause metallic fatigue failure. The energy overhead should be a function of the bending angle θ, the shaft rotating speed (or frequency f) and the rigidity of the shaft material. Since f was set to 83.3 Hz and did not vary much and

the shaft material does not change, the energy overhead was modeled as a polynomial of θ and calibrated.

Controlling the grinding angle might be a more serious problem. It was difficult to control the bending angle and grinding angle simultaneously because of the flexibility and structural specialty of the bending section. It was also difficult to keep the grinding stone in full contact with the workpiece surface throughout an entire grinding task, unlike traditional machining, where the grinding angle could be precisely controlled. The variation of grinding angle influenced the MRR significantly. The inability to directly measure the grinding angle or accurately calculate it from $F_{Loadcell}$ and δ_{LVDT} was one major source of error in MRR prediction results. In crack smoothing applications spherical grinding tool head is a possible alternative to cylinder grinding stone to reduce this error.

Chapter 5

Conclusions

5.1 Summary

The hypothesis that the endoscopic tool can be used to remove a predetermined amount of material has been studied.

In chapter 1, a literature review was conducted to reveal the endoscopic technique advancements in both medical and industry practices. Patents of using endoscope as a machining tool and novel methods of more complex endoscopic application in surgery have been found.

In chapter 2, static characteristics of the endoscopic tool was studied. A geometric model and a static force model were built to estimate the pose of the endoscopic tool and the external normal force exerted on the tool head.

In chapter 3, dynamic properties of the endoscopic tool was studied. A dynamic model was built to find the fundamental frequency of the tool. Regenerative chatter theory was applied on the tool for chatter prediction. Finally, a chatter detection method was proposed for online chatter detection in endoscopic grinding process.

In chapter 4, a material removal prediction model was built using semi analytical and semi empirical method, and the repeatability was validated.

5.2 Conclusions

It was found that the pose and force on the flexible endoscopic tool could be reasonably estimated and tracked during machining operation. The average error of pose estimation model was less than 4mm in bending section tip position and 5 degrees in bending section orientation. The force prediction model had an average prediction accuracy of 0.5 N and the error might be larger

than 5 N in worst case. The error in the predictions could be reduced by calibrating the model for comprehensive configurations through more experiments (using automatic test and measurement system), using precise tracking equipment as a more accurate reference channel, design a more predictable bending section and incorporate with high accurate sensors.

From the dynamic study it was found that the fundamental frequency of the endoscopic tool was 13 Hz. It was shown that the endoscopic tool has a low fundamental frequency, in the range of 1 to 100 Hz, so increasing the grinding speed could help stabilize the tool and achieve higher MRR. The only concern is that current power transmission shaft might break due to fatigue induced by high rotational speed and large bending angle. It was found that the dynamic characteristics of the flexible machining system were sensitive to the method of machining and power transmission, and these could be studied in future work.

Material removal prediction model showed that in 2D configuration, the average prediction error is 22% for the 18 samples tested. Whether this number is acceptable will depend on the specific application. The error can be reduced if the grinding angle is known or negligible, therefore sphere grinding stone could be used to improve this. The results revealed that when bending angle is small and normal force is small, chatter will occupy a large percent of grinding energy. When normal force is large and bending angle is large, the power transmission overhead will become the dominant factor of wasted energy.

The final conclusion is that the amount of material removed can be predicted in a flexible, endoscopic machining operation. The results suggest that it should be possible to remove a predetermined amount of material from a workpiece with better control and precision of the machine tool. The accuracy of the material removal depended on the accuracy of the bending section, sensors, endoscopic tool (head), and models.

5.3 Contributions

In this research endoscopic (force critical) machining was proved feasible. The following contributions were made to the concept of non-rigid machining:

1. The methods of pose estimation under forced condition and static force prediction was formulated for an endoscopic tool.

2. Traditional machining dynamic analysis revealed the dynamic characteristics of a non-rigid machining process.

3. The method for prediction of amount of material removed was created and validated for non-rigid machining. The energy based, material removal model was built, quantitatively studied, and shown to have reasonable accuracy.

5.4 Discussion

Since most objects (made of metals) with a three dimensional internal geometry, such as turbine engine, would not be conducive to X-ray or CT-scan, three-dimensional position and orientation mapping are of great importance when using endoscope to machining interior surface of these objects. One possible solution is using robotic approach to measure the joint angle of each joint. The difficulty is that the limited volume of bending section might not be able to hold dozens of angle sensors.

Since there are couplings [23] in the horizontal and vertical degree of freedom of the bending section, it should be difficult to estimate the 3D position of a traditional endoscope bending section by using two or more LVDT sensors and load cells. Another approach is to build a new bending section with uncoupled degrees of freedom and more predictable geometric configuration.

It is well known that high speed grinding can improve MRR and reduce chatter at the same time. Low profile grinding stone working at very high speed, say 300K rpm will enable endoscopic grinding tool with promising material removal capability. However, power transmission shaft will suffer from significant metallic fatigue rotating at such a high speed. Alternative solutions will be using a pneumatic driven tool head, just like the dental drill, or substitute the big external motor and the power transmission shaft with a small motor module directly installed on the tip of bending section.

5.5 Future Work

In the future, new bending section with more predictable structure could be built. The connection between tool head and the endoscope should be modularized to ease the switching of different tool heads. Two sets of LVDT and load cell sensors could be installed to accomplish three dimension pose estimate and MRR prediction.

Chapter 6

Acknowledgment

First I offer my sincerest gratitude to my supervisor, Professor Scott Miller, who encouraged and guided me through my academic program. He is a good mentor and a good friend as well. Thank you.

This thesis could not have been completed without my thesis committee – Professor Peter Berkelman and Professor Brian Bingham. Their enlightening questions, insightful suggestions, comments and revisions helped me finish the last and the most crucial step of my academic journey.

I would like to acknowledge and extend my heartfelt gratitude to the department chair – Professor Mehrdad N. Ghasemi Nejhad, the graduate chair – Professor B. H. Chao. and emeritus professor Ronald H. Knapp.

It is my great pleasure to thank our department secretary Ms. Joanne Yee. She is alway very kind, patient and highly effective to solve any administrative issues.

I am grateful to my classmates, labmates, colleagues and friends Meng Cai, Stephan Fabel, Hamed Eksiri, Kusada Kentaro, Chamil Viranga, Peng Hu, Xiudong Xie, Mian Cui, Dr. Raghu Srinivasan, Dr. Chad Liu, Dr. Wei Lu, Dr. Kang Xie, Dr. Jiwei He, Dr. Ji Ma and many others whose names are not listed here. They lent me substantial help on my way to today's academic achievement.

I wish to thank my entire extended family for providing a loving environment to me. I also owe my deepest gratitude to my girlfriend Yihong Liu, who supports and encourages me all the way through this studying abroad journey.

Lastly, I wish to thank my parents Cheng Sheng Lei and Ling Ma, and my most loved and be loved grandma Xiao Juan Li. I will be always love you. To them I dedicate this thesis.

Bibliography

[1] Moeller. Grinding apparatus for blending deffects on turbine blades and associated method of use, May 2005.

[2] Diener. Instrument for working the surfaces of parts inside engineered cavities, December 1995.

[3] Desgranges. Apparatus for retouching, in situ, components such as the rotor blades of a turbomachine, and a retoughing, method using the appraratus., April 1992.

[4] Pratt & Whitney. Pratt & whitney wins maintenance contract for rolls-royce engines on harrier fighters. Technical report, 2002. URL `http://www.pw.utc.com/media_center/press_releases/2002/07_jul/7-21-2002_8512115.asp`.

[5] Silvia Seng. Turbine engine fan disk crack detection test. Final Report DOT/FAA/AR-04/28, Naval Air Warfare Center, Weapons Division, Weapons Survivability Laboratory, China Lake, CA, September 2004.

[6] Harland S. Winter. *Pediatric Gastrointestinal Endoscopy: Textbook And Atlas*. BC Decker Inc. (U.S.), 1st edition, December 2005.

[7] VisionScope Technologies. Industrial inspection and endoscope uses. Web, June 2011.

[8] F. Arai, D. Azuma, K. Narumi, Y. Yamanish, and Yu-Ching Lin;. Design and fabrication of a shape memory alloy actuated exoskeletal microarm. pages 339–343, Nagoya, Japan, November 2007. 2007 International Symposium on Micro-NanoMechatronics and Human Science, MHS.

[9] H. M. G. Hussein. Endoscopic device (us patent no. 4470407), 1984.

[10] Fujinon. Double balloon endoscopy. Web source, 2009. URL `http://www.fujinonendoscopy.com/default.aspx?pageid=210`.

[11] Olympus. Single balloon enteroscopy system. Web, 2011. URL http://www.olympusamerica.com/msg_section/msg_product.asp?p=3&sc=1&product=1298&fl=24.

[12] M. H. Raibert and J. J. Craig. Hybrid position/force control of manipulators. *Journal of Dynamic Systems, Measurement and Control, Transactions of the ASME*, 103(2):126–133, 1981.

[13] Ali Akbar Akbari and Shizuichi Higuchi. Autonomous tool adjustment in robotic grinding. *Journal of Materials Processing Technology*, 127(2):274–279, September 30 2002. doi: 10.1016/S0924-0136(02)00156-5.

[14] Shin-Ichi Matsuoka, Kazunori Shimizu, Nobuyuki Yamazaki, and Yoshinari Oki. High-speed end milling of an articulated robot and its characteristics. *Journal of Materials Processing Technology*, 95(1-3):83–89, October 1999. doi: 10.1016/S0924-0136(99)00315-5.

[15] M. Yu, J. Zhao, L Zhang, and Y Wang. Study on the dynamic characteristics of a virtual-axis hybrid polishing machine tool by flexible multibody dynamics. *Proceedings of the Institution of Mechanical Engineers, Part B: Journal of Engineering Manufacture*, 218(9):1067–1076, September 2004. doi: 10.1243/0954405041897167.

[16] Jerzy Plosa and Stanislaw Wojciech. Dynamics of systems with changing configuration and with flexible beam-like links. *Mechanism and Machine Theory*, 35(11):1515–1534, November 2000. doi: 10.1016/S0094-114X(00)00014-8.

[17] Hui Zhang, Jianjun Wang, George Zhang, Gau Zhongxue, and etc. Machining with flexible manipulator: Toward improving robotic machining performance. In *IEEE/ASME International Conference on Advanced Intelligent Mechatronics, AIM*, volume 2, pages 1127–1132, 2005.

[18] Koji Ikuta, Takahiko Hasegawa, and Shinichi Daifu. Hyper redundant miniature manipulator "hyper finger" for remote minimally invasive surgery in deep area. In *Proceedings - IEEE International Conference on Robotics and Automation*, volume 1, pages 1098–1102, Taipei, Taiwan, September 2003. Institute of Electrical and Electronics Engineers Inc. doi: 10.1109/ROBOT.2003.1241739.

[19] Shigeo Hirose and Richard Chu. Development of a light weight torque limiting m-drive actuator for hyper redundant manipulator float arm. Proc. IEEE Int. on Robotics and Automation, pages 2831–2836, 1999.

[20] Shigeo Hirose and Edwardo Fukushima. Snakes and strings: New robotic components for rescue operations. *International Journal of Robotics Research*, 23(4-5):341–349, April/May 2004. doi: 10.1177/0278364904042202.

[21] Amir Degani, Howie Choset, Alon Wolf, and Macro Zenati. Highly articulated robotic probe for minimally invasive surgery. In *Proceedings - IEEE International Conference on Robotics and Automation*, volume 2006, pages 4167–4172, 2006. doi: 10.1109/ROBOT.2006.1642343.

[22] C. A. Mosse, T. N. Mills, G. D. Bell, and C. P. Swain. Device for measuring the forces exerted on the shaft of an endoscope during colonoscopy. *Medical & Biological Engineering & Computing*, 36:186–190, March 1998.

[23] H. Lipkin and J. Munnae. Endoscope geometrical analysis and kinematic control. volume 8 of *Proc. of the ASME International Design Engineering Technical Conferences and Computers and Information in Engineering Conference*, pages 231–238, 2007.

[24] C. Steger, Ulrich M., and Wiedemann C.. *Machine Vision Algorithms and Applications*. Wiley-VCH, 1st edition, 2008.

[25] L. Gl. Shapiro and G. C. Stockman. *Computer Vision*. Prentice Hall, 2001.

[26] Warren. R. DeVries. *Analysis of Material Removal Processes*. Springer-Verlag, 1991. ISBN 0-387-97728-7.

[27] S. Malkin. *Grinding Technology Theory and Applications of Machining with Abrasives*. Ellis Horwood Series in Mechanical Engineering. Ellis Horwood Limited, Chichester, West Sussex, PO19 1EB, England, 1st edition, 1989.

[28] H. Li and Y. C. Shin. A comprehensive dynamic end milling simulation model. *ASME J. Manuf. Sci. Eng.*, 128:86–95, 2006.

[29] B. Rao and Y. C. Shin. A comprehensive dynamic cutting force model for chatter prediction in turning. *Int. J. Mach. Tools Manufact.*, 39(10):1631–1654, 1999.

[30] B. E. Clancy and Y. C. Shin. A comprehensive chatter prediction model for face turning operation including the tool wear effect. *Int. J. Mach. Tools Manufact.*, 42(9):1035–1044, 2002.

[31] Sanjiv G. Tewani, Keith Rouch, and Bruce L. Walcott. A study of cutting process stability of a boring bar with active dynamic absorber. *Int. J. Mach. Tools Manufact.*, 35(1):91–108, 1995.

[32] C. Mei. Active regenerative chatter suppression during boring manufacturing process. *Robotics and Computer-Integrated Manufacturing*, 21:153–158, 2004. doi: 10.1016/j.rcim.2004.07.011.

[33] Deqin Mei, Tianrong Kong, Albert Shih, and Zichen Chen. Magnetheological fluid-controlled boring bar for chatter suppression. *Journal of Materials Processing Technology*, 209:1861–1870, 2009. doi: 10.1016/j.jmatprotec.2008.04.037.

[34] I. Inasaki, B. Karpuschewski, and H. S. Lee. Grinding chatter - origin and suppression. *CIRP Annals - Manufacturing Technology*, 50(2):515–534, 2001. ISSN 00078506. doi: 10.1115/1.2118748.

[35] E. Govekar, A. Baus, J. Gradisek, F. Klocke, and I. Grabec. A new method for chatter detection in grinding. *CIRP Annals - Manufacturing Technology*, 51(1):267–270, 2002. ISSN 00078506.

[36] Janez Gradisek, A. Baus, E. Govekar, Fritz Klocke, and Igor Grabec. Automatic chatter detection in grinding. *International Journal of Machine Tools and Manufacture*, 43(14):1397–1403, 2003. doi: 10.1016/S0890-6955(03)00184-6.

[37] Lei Wang and Ming Liang. Chatter detection based on probability distribution of wavelet modulus maxima. *Robotics and Computer-Integrated Manufacturing*, 26(6):989–998, 2009. doi: 10.1016/j.rcim.2009.04.011.

[38] Emad Al-Regib and Jun Ni. Chatter detection in machining using nonlinear energy operator. *Journal of Dynamic Systems, Measurement and Control, Transactions of the ASME*, 132(3):1–4, May 2010. ISSN 00220434. doi: 10.1115/1.4001331.

[39] Hongqi Li and Y. C. Shin. A time-domain dynamic model for chatter prediction of cylindrical plunge grinding processces. *Trans. of the ASME*, 128:404–415, 2006. doi: 10.1115/1.2118748.

[40] Y. C. Shin and A. J. Waters. Face milling process modeling with structural nonlinearity. *Trans. North American Manufacturing Research Institution of SME*, 22:157–163, 1994.

[41] Y. S. Tarng and T. C. Li. Detection and suppression of drilling chatter. *Journal of Dynamic Systems, Measurement and Control, Transactions of the ASME*, 116(4):729–734, 1994.

[42] Y. S. Tarng and T. C. Li. Adaptive pattern recognition of drilling chatter. *Journal of Materials Processing Technology*, 48(1-4):247–253, Jan 1995. doi: 10.1016/0924-0136(94)01656-L.

[43] Geoffrey Boothroyd and Winston A. Knight. *Fundamentals of Machining and Machine Tools (2nd Edition)*. Marcel Dekker, Inc., 2 edition, 1989.

[44] R. Snoeys and D. Brown. Dominating parameters in grinding wheel and workpiece regenerative chatter. In *Proc. of the 10th Int. MTDR Conference*, pages 325–348, Manchester, 1969.

[45] J. G. Wager, R. J. Baylis, and B. J. Stone. The build up and decay of vibration during grinding. *Annals of the CIRP*, 32(1):255–259, 1983. doi: 10.1016/S0007-8506(07)63402-7.

[46] K. Steffens and H. Follinger. A new approach for investigating dynamic effects in grinding. volume 34 of *CIRP Annals 1985: Manufacturing Technology, Annals of the International Institution for Production Engineering Research. 35th General Assembly of CIRP.*, pages 267–270. Technische Rundschau, Berne, Switz, 1985.

[47] H. K. Tonshoff, J. Peters, I. Inasaki, and T. Paul. Modelling and simulation of grinding process. *CIRP Annals - Manufacturing Technology*, 41(2):677–688, 1992. ISSN 00078506.

[48] John J. Craig. *Introduction to Robotics Mechanics and Control*. Pearson Education International, 3rd edition, 2004. ISBN 0-13-123629-6.

[49] T. Thomessen, T. K. Lien, and P. K. Sannaes. Robot control system for grinding of large hydro power turbines. *Industrial Robot*, 28(4):328–334, 2001. doi: 10.1108/01439910110397183.

[50] Zengxi Pan, Hui Zhang, Zhenqi Zhu, and Jianjun Wang. Chatter analysisi of robotic machining process. *Journal of Materials Processing Technology*, 173(3):301–309, April 2006. doi: 10.1016/j.jmatprotec.2005.11.033.

[51] Zengxi Pan and Hui Zhang. Analysis and suppression of chatter in robotic machining process. In *ICCAS 2007 – International Conference on Control, Automation and Systems*, number 4407093, pages 595–600, Seoul, Korea, 2007. Inst. of Elec. and Elec. Eng. Computer Society. doi: 10.1109/ICCAS.2007.4407093.

[52] J. Tlusty and M. Polacek. The stability of machine tools against self-excited vibrations in machining. *ASME International Research in Production Engineering*, pages 465–474, 1963.

[53] S. A. Tobias and W. Fishwick. The chatter of lathe tools under orthogonal cutting conditions. *Transactions of the ASME*, 80:1079–1088, 1958.

[54] S. A. Tobias. *Machine Tool Vibration.* Blackie, London, UK, 1965.

[55] Ronald Faassen. *Chatter Prediction and Control for High-Speed Milling: Modelling and Experiments*. PhD thesis, Eindhoven University of Technology, 2007.

[56] Jianping Yue. Creating a stability lobe diagram. In *Proceedings of the 2006 IJME*, INTERTECH Conference, 2006.

[57] Tony L. Schmitz and Kevin S. Smith. *Machine Dynamics Frequency Response to Improved Productivity*. Springer, 2009. ISBN 978-0-387-09644-5. doi: 10.1007/978-0-387-09645-2.

[58] *KISTLER 9272 Dynamometer Datasheet*. Kistler Instrumente AG, PO Box, Eulachstr. 22, CH-8408 Winterthur, 9272_000-153e-11.05 edition, 2005.

[59] *KISTLER 5010B Charge Amplifier Datasheet*. Kistler Instrumente Corporation, 75 John Glenn Dr., Amherst, NY 14228, 5010b_000-387 07.09 edition, 2009.

[60] MACRO SENSORS. *SE 750 Series General Purpose DC-LVDT Position Sensors Technical Bulletin 1019*. Division Of Howard A. Schaevitz Technologies, Inc., 7300 US Route 130 North, Bldg. 22, Pennsauken, NJ 08110-1541 USA, 2007.

[61] Web resource. Dental drill. http://www.discoveriesinmedicine.com/Com-En/Dental-Drill.html, May 2011.

[62] Ioan D. Marinescu and Boris Dimitrov. *Tribology of Abrasive Machining Process*. William Andrew, 1st edition, 2004.

[63] Hui Zhang and Zengxi Pan. Robotic machining: Material removal rate control with a flexible manipulator. In *2008 IEEE International Conference on Robotics, Automation and Mechatronics, RAM 2008*, number 4690881, pages 30–35. Inst. of Elec. and Elec. Eng. Computer Society, 445 Hoes Lane - P.O.Box 1331, Piscataway, NJ 08855-1331, United States, September 2008.

[64] Yixu Song, Wei Liang, and Yang Yang. A method for grinding removal control of a robot belt grinding system. *Journal of Intelligent Manufacturing*, pages 1–11, 2011. doi: 10.1007/s10845-011-0508-6.

[65] S. Kannappan and S. Malkin. Effects of grain size and operating parameters on the mechanics of grinding. *Journal of Engineering Industry Transaction ASME*, 94(3):833–842, August 1972.